I. M. Rizwanul Fattah, C. Ming, Q. N. Chan, A. Wehrfritz, P. X. Pham, W. Yang, S. Kook, P. R. Medwell, G. H. Yeoh, E. R. Hawkes, and A. R. Masri

Spray and combustion investigation of post injections under low temperature combustion conditions with biodiesel

Energy and Fuels, 2018; 32(8):8727-8742

Spray and Combustion Investigation of Post Injections under Low Temperature Combustion Conditions with Biodiesel

I. M. Rizwanul Fattah,† C. Ming,† Q. N. Chan,*,† A. Wehrfritz,† P. X. Pham,‡ W. Yang,¶ S. Kook,† P. R. Medwell,§ G. H. Yeoh,† E. R. Hawkes,†,∥ and A. R. Masri‡

†*School of Mechanical and Manufacturing Engineering, UNSW Sydney, NSW 2052, Australia*

‡*School of Aerospace, Mechanical and Mechatronic Engineering, The University of Sydney, NSW 2006, Australia*

¶*School of Chemical and Materials Engineering, Hefei University, Anhui 230601, PR China*

§*School of Mechanical Engineering, The University of Adelaide, SA 5000, Australia*

∥*School of Photovoltaic and Renewable Energy Engineering, UNSW Sydney, NSW 2052, Australia*

E-mail: qing.chan@unsw.edu.au

Abstract

Post injection is a multiple injection strategy that is commonly used as a particulate matter control measure to reduce soot emissions, yet the mechanisms and the interactions between the main and post injections are only vaguely understood. For this work, experiments were performed to assess the effects of varying dwell time between the main and post injections in a compression-ignition (CI) engine environment simulated using a constant-volume combustion chamber (CVCC). The ambient density, bulk temperature and oxygen concentration used for this work were controlled at 19.4 kg/m^3, 900 K and 15 vol.% O_2, respectively. A canola oil based biodiesel was tested and injected at a fixed injection pressure of 100 MPa into the simulated CI engine environment. A mass ratio of 80% to 20% was maintained between the main and post injections, with the dwell time between the injections varied from 1.5 to 2.5 ms. Comparative measurements were performed using the same fuel and injection schedules, but at a higher ambient gas temperature condition of 1100 K. Optical diagnostics methods, including diffused-back illumination and high-speed flame luminosity imaging, were used to assess the spray and combustion processes of the post injection test case. Under the conditions of this work, it was found that the ignition delays, ignition locations and the flame lift-off lengths of the post injection flames are consistently shorter than those of the main injections, with the variations influenced by the extent of the interaction of the post injection with the combustion products from the main injection. Two-color pyrometry technique was also used to measure the soot temperature and soot concentration factor information of the main-post injections cases. The data revealed a greater interaction between the main and post injections resulted in a more rapid development of the soot zone of the post injection with higher temperature, after ignition. The distribution of the most probable soot concentration factors of the post injection was also found to be narrower, with lower soot content values.

1 Introduction

The continuous need to maximize fuel economy and engine power whilst minimizing emissions intensifies the call for innovative combustion and after-treatment technologies. The development and implementation of injection systems that are capable of advanced injection strategies, such as multiple injection, which began in the early 1990s,[1] paved the way for considerable research[2–4] and interest into the application of such strategies. Since then, multiple injection strategies are commonly employed in modern engines to achieve a range of improvements, such as refined engine control, reduced combustion noise, lower soot production and/or enhanced soot oxidation.[5–8]

Post injection is a multiple injection strategy that involves the introduction of a small quantity of fuel after the end of main injection event. The post injection strategy is generally used as a measure to reduce soot emissions, or to enable exhaust gas after-treatment technologies.[9,10] Questions, however, remain about the mechanisms through which reduced pollutant emissions is achieved, and whether interactions between the combustion of main and post injections contribute to the observed outcomes.[9,11] For example, previous studies[11,12] have reported that the enhanced mixing induced by the post injection can bring fresh oxygen to the soot from the main injection to increase soot oxidation. Other works[11,13] have noted that the additional heat release, induced by post injection, can elevate in-cylinder temperature conditions to promote soot oxidation. Several studies,[14,15] on the other hand, have attributed the reduced exhaust soot emission to the suppression of soot formation that arose from the discontinuous introduction of the fuel through a series of smaller injection processes. The different findings presented in the literature imply that the mechanisms and the interactions between the injections can vary, depending on the injection schedule, the fuel type and the ambient conditions under which the post injection occurred. A better understanding of the mechanisms associated with various operating conditions is therefore critical to enable consistent, effective implementation of the post injection strategy.[5]

In addition to multiple injection strategies, the use of alternative fuels, such as biodiesels, is also a promising viable approach to reduce particulate matter, CO and unburned hydrocarbon emissions, when compared with conventional diesel fuel. Whilst the use of biodiesels has been reported to cause an increase in NOx emission, this issue can be alleviated by using biodiesels in low-temperature combustion (LTC) mode.[16] Several studies have looked into combining LTC modes, multiple injection strategies and alternative fuels to achieve further engine performance improvement and emissions reduction.[16,17] However, depending on their feed stocks,[18] biodiesels can have different properties that would impact on the fuel atomization, evaporation, combustion and pollutant formation processes.[17,19] As such, whilst significant benefits can be achieved, they can only be realized through improved understanding of the mechanisms involved with different combinations of multiple injection strategies, combustion conditions, and fuels.

This work aims to improve the understanding associated with the implementation of post injection strategy, when used in conjunction with biodiesel under LTC condition, with a focus on the interaction between the main and post injections for selected main-post injection schedules. Canola oil based biodiesel fuel with well-known composition was injected into a simulated compression-ignition (CI) engine condition with 19.4 kg/m^3 ambient density, 5.1 MPa ambient pressure, 900 K bulk temperature and 15 vol.% O_2 concentration, inside an optically-accessible constant volume combustion chamber (CVCC). It is noted that in engine experiments, changes that are made to the operating parameters, such as intake temperature, intake pressure, engine speed and engine load, would often result in simultaneous changing in several basic parameters of the engine, such as ambient temperature, density, pressure and injection timing.[20] This has resulted in some challenges in isolating the effect of basic parameters on the spray or combustion events of interest for detailed understanding, when interpreting engine data. For this work, the experiments are therefore performed in a CVCC, which is capable of providing more accurate and direct control of the basic parameters.[21] It is also noted that the experimental conditions were selected for this work so that free jets can be generated. This is to avoid the complexities that can arise from flame-wall interaction – a phenomenon that remains only vaguely known, due to the multitude and complexity of the associated processes.[22] The advanced understanding that is derived from the free jet experiments, nevertheless, is still useful to help the research community to better understand the basic processes affecting main-post injections, which in turn, can be extended to results in more complex and realistic engine scenarios. The canola oil based biodiesel is of interest to this work as it has been previously investigated by the authors under open flame burner, performance engine and CVCC settings.[23,24] The biodiesel, which has been shown to be sooting even under moderate exhaust gas recirculation (EGR) conditions, is selected for post injection as a soot reduction approach.[24] The mass ratio of the main to post injection was maintained at 80% and 20% throughout the experiment. For this work, the dwell time, and hence the coupling between the main and post injections, was varied to examine its effects on the spray and combustion properties. A high-speed digital camera was used to record the flame luminosity and two-color images from the combustion events. A detailed analysis was performed on the flame images recorded to characterize the main-post combustion properties, including ignition delay, ignition location, and flame lift-off lengths, in addition to soot temperature and soot concentration factor (KL) distributions measured using two-color pyrometry. The liquid spray and length information of the main and post injections were also characterized in non-reacting environment simulated using the CVCC. In addition, to examine the sensitivity of the results to the variation in ambient temperature, comparative measurements were repeated at a higher ambient gas temperature condition of 1100 K that is known to increase soot formation,[25] but with the same fuel and injection schedules.

2 Experimental Details

2.1 Constant-volume Combustion Chamber

The experiments were conducted in an optically-accessible CVCC at UNSW Sydney, under simulated CI engine condition. A schematic diagram of the chamber, along with the high-speed flame luminosity imaging setup, is provided in Fig. 1. The vessel has a cubical combustion chamber, 114 mm on each side, with optical access provided by side-port windows (102 mm diameter). A single-hole solenoid fuel injector was mounted at the center of a metal side-port of the CVCC. An agitator was mounted at the top of the CVCC and was used to maintain a spatially uniform temperature environment in the chamber. The CI engine condition within the chamber was simulated by metering acetylene, hydrogen, oxygen and nitrogen gases into the CVCC. The combustible gas mixture was subsequently spark-ignited to create a high temperature and pressure environment. Following the premixed combustion, the combustion products inside the chamber were allowed to cool down through heat transfer to the cooler chamber wall, during which the pressure inside the chamber was monitored with a pressure sensor (Kistler 6052C). For this work, an ambient condition with gas density, pressure and temperature of 19.4 kg/m^3, 5.1 MPa and 900 K, respectively, was targeted. The fuel injector was triggered once the targeted condition was reached. The metering of the reactant gas was also controlled so that an environment with 0 or 15 vol.% oxygen concentration can be generated after the premixed combustion process. The 0 vol.% ambient oxygen concentration (non-reacting) condition was used to provide insights into the liquid length penetration characteristics of the sprays with varied injection schedules, without the complex effects of heat release from the combustion processes. The 15 vol.% (reacting) ambient oxygen environment was selected to mimic operating condition for modern compression-ignition engines that use moderate EGR and have minimal NOx emissions.[25] For comparison purpose, measurements were also repeated under the same ambient condition, but at a higher ambient temperature of 1100 K. A summary of the ambient experimental condition for this work is listed in Table 1.

A Bosch common-rail (CP4) system with a single-hole solenoid injector (105 µm) was used as the fuel injection system. A common-rail PCV driver (Zenobalti, ZB-1200) was used to regulate and maintain the injection pressure at 100 MPa. In addition, an injection driver (Zenobalti, ZB-5100) was used in conjunction with a digital delay generator (Stanford Research Systems DG 535) to control the triggering of the fuel injection system. The single-hole injector was used to avoid the complexity that can arise from jet-jet interaction. In this work, the multiple injection case was tailored to represent a 'main plus post' injection schedule, with a total injected fuel mass of 10 mg. A single injection case, with its injection duration adjusted so that it has a total injected fuel mass as the main-post injection case, was also measured for reference purpose. The rate of injection (ROI) profiles of the main-post and single injection cases were measured using a Bosch tube type injection rate meter. The fuel mass ratio of the main to post injections was fixed as 80% to 20%. Dwell time (DT), which is defined here as the time between the end of electronic command of the main and the actual start of injection for the post, was set as 1.5, 2.0 and 2.5 ms for the main-post cases. It is noted that the shortest DT used (1.5 ms) is near the limit of the injector capability, for which the solenoid valve and needle lift can be actuated reliably. A summary of the fuel injection conditions is provided in Table 1.

It is noted that this work is part of a larger project that is aimed at improving the understanding of the combustion and pollutant emission characteristics of biodiesels. In the authors' previous work,[23,26,27] four surrogate biodiesel fuels, which were abbreviated as C810, C1214, C1618 and C1875 in previous publications, comprised of fatty acid methyl esters (FAMEs) that are derived from palmera-based and coconut-based oils (C810, C1214), pale-based oil (C1618), and canola-based oil (C1875), respectively, were examined as they have physico-chemical properties that are adequate to represent biodiesels from a broad range of feed stocks. Biodiesels C810 and C1214 are representatives of saturated FAMEs with short and medium carbon chain lengths. Specifically, biodiesels C1618 and C1875, on the other hand, have long and similar chain lengths but with different saturation degree; with C1618 being partially saturated and C1875 being almost fully unsaturated. These differences in the molecular structures have been previously shown to affect the physical and chemical mechanisms that occur during combustion, and are correlated with the ensuing engine performance and pollutant emission trends. The C1875 fuel, which has highest soot propensity amongst the four surrogate fuels because of its long carbon chain and low degree of saturation, has been shown to be reasonably sooty even at moderate EGR condition, and is therefore selected for this post injection for soot reduction study under exhaust gas recirculation condition. A detailed description of the fuel can be found in Ref.[23] and therefore, only a short summary the main compositions and properties of the biodiesel is provided in Table 1. In brief, the biodiesel fuel used has an oxygen content, iodine, saponification and cetane numbers of 10.83 wt%, 105, 185 and 59, respectively. The iodine and saponification numbers of the fuel indicate that it is almost unsaturated and has a long carbon chain length. The high cetane number, on the other hand, implies that the fuel has a short ignition delay.

2.2 Optical Diagnostics

Two optical techniques were used for this work, namely diffused-back illumination (DBI) and high-speed natural flame luminosity imaging. For both of these optical diagnostic methods, which were not performed simultaneously, a high-speed camera (Photron SA-5) that was equipped with a 85 mm f#1.8 Nikkor lens, was used to record the events. The f-stop of the camera lens and the exposure time of the camera were adjusted between the DBI and high-speed flame luminosity imaging setups to ensure a good balance between optimum light level and camera exposure. For the DBI imaging, the collimated light output from a continuous, high-powered LED that was emitting at a central wavelength of 455 nm, was used for illumination. An engineered diffuser was also placed between the light source and the spray to ensure homogenized illumination. The camera, which was positioned directly opposite to the LED light source, was operated at a frame rate of 15,000 frames per second (fps), with 1 µs exposure and a pixel resolution of $\sim$0.14 mm per pixel. For the high-speed flame luminosity imaging, the time-resolved flame images of the combustion of multiple and single injection cases were captured using the high-speed camera, which was also operated at the same frame speed and exposure time. The pixel resolution of the image was $\sim$0.2 mm per pixel. Typical time sequenced flame luminosity images recorded for a main-post injection case, with a dwell time of 1.5 ms, are presented in Fig. 2. It is noted that for both DBI and high-speed flame luminosity imaging, the camera was synchronized to the start of injection of the injector. At least five runs were performed for each test condition to ensure good repeatability, and at least 150 images were recorded for each run, to ensure that entire combustion event was captured.

3 Image post-processing

3.1 Diffused back illumination imaging post-processing

To determine the spatial extent of the liquid phase in the DBI images, the light intensity, I, at a pixel location from an image with spray, was compared against the background intensity, I_o, at the same pixel location from an image with no spray. To determine the cut-off I/I_o value suitable for use to derive liquid length information from the DBI images, both DBI and Mie-scattering images were recorded for a series of evaporating sprays under test conditions that are similar to this work. The Mie-scattering images obtained was first processed to derive liquid boundary information. It is noted that an image intensity value that corresponds to 3% of the maximum intensity, which was widely used as the threshold setting for the processing of Mie-scattering images in the literature,[28,29] is also applied here for consistency reason. A systematic variation of the I/I_o cut-off value used to process the DBI images of the same sprays was then performed. A threshold value of 0.3 was found to give the most consistent agreement between both techniques, and is therefore used for this work. It is noted that the Mie-scattering imaging was performed using high-speed camera imaging with side illumination, and was only used for the calibration of the DBI results. A schematic diagram of the DBI and Mie-scattering imaging setups, and their orientations in relation to the chamber, is shown in Fig. 3.

3.2 Flame luminosity imaging post-processing

A novel color band approach, which was first introduced by Larsson[30] and further expanded upon by Svensson *et al.*[31] was implemented to provide soot temperature and soot KL (a factor that is proportional to the soot volume fraction and gas layer thickness[31,32]) information. The color band approach, which only requires the use of a single digital color camera for soot two-color measurements, has the advantage of avoiding introducing errors due to potential misalignment of frames taken by two cameras and eliminates the need for complex optics that are typically required for the more classical implementation of two-color pyrometry technique. The general two-color thermometry theory has been detailed in the literature[31–33] and is therefore not described in detail here. In essence, for each pixel, a modified Planck's blackbody function, which incorporates wavelength-dependent soot emissivity model and responsivity of the detection system used (optics train, filter and high-speed camera), was applied to the red and green color bands to yield two equations with two unknowns (*e.g.*, the soot temperature and soot KL factor). The optical response of the high-speed camera used, for each of its color channel, is shown in Fig. 4. The technique was subsequently calibrated against a tungsten lamp with known spectral properties.

Following the approach of Zha *et al.*,[32] to reduce the computational time during image processing, two universal surfaces (Fig. 5) that map the domains of the red and green pixel intensities to soot temperature and KL surfaces, were generated. By matching the pixel intensities recorded for the red and green channels to the parameter spaces of the universal surfaces, the solutions to the two equations can be sought in a time-efficient manner. It should be noted that the two-color pyrometry technique is a line-of-sight method and therefore, the optical signals detected are inherently integrated along the optical path.[31,34] In previous studies,[31,34] the accuracy of the two-color technique has been observed to be highly susceptible towards the spatial gradients in soot properties, especially temperature, in the optical path. Additionally, the deduced two-color temperature and soot concentration values have been shown to be biased towards soot within the hot flame surface that is closest to the camera.[31] For example, Musculus *et al.*[34] have reported that the two-color technique can overestimate the actual soot temperature by 200 K, whilst underestimating the true soot concentration by 50%. In a separate previous study by Svensson *et al.*,[31] it was shown that the two-color technique can have a temperature uncertainty in the range of ∼150 K, and is only reliable for qualitative soot concentration measurement. It is therefore necessary to consider all these limitations, when interpreting the two-color data obtained.

4 Results and discussion

4.1 Liquid penetration lengths

The quasi-steady liquid length measurements of the main-post injections with single injection case are presented and compared in Fig. 6, to give insights into the potential effects of DTs on the characteristics of the liquid phase. It should be noted that both the liquid penetration measurements were performed under high-temperature, high-pressure but inert (0% ambient oxygen) conditions, as this would help to eliminate the uncertainty associated with heat-release effects on liquid penetration, and permit comparison with previous liquid length studies.[35] The average liquid lengths of the sprays are observed to be relatively stable across the stabilized periods of their injections, albeit with slight fluctuations (22%). The liquid lengths of the main injections of the multiple injection cases are also found to similar to that measured for the single injection case. Together, these findings imply that sufficient quantities of fuel were injected during the main injection periods of the multiple injection cases to reach quasi-steady liquid lengths. From the figure, it can also be seen that the maximum liquid penetrations of the post injections are comparable to that of the corresponding main injections and are not found to be sensitive towards the variation in DT, especially considering the experimental uncertainty. The liquid penetration profiles of the post injections, however, are observed to vary with changing DT. Specifically, from the liquid penetration profiles of the post injections, it can be seen that the time that is required for the post injection to reach the maximum liquid penetration distance is found to increase with increasing DT. It is noted that similar observations were also reported in a previous study.[35] In that study, it was shown that the penetration rate of the second injection can be greater than the first injection, because the second enters into cool, fuel-laden mixture region left by the first.[35] It should be noted it is unclear if these spray characteristics would be observable in reactive ambient conditions.

4.2 Flame luminosity plots

To visualize the effects of the DT on the combustion characteristics, radial integration of the flame luminosity at each axial location of each frame was performed for the high-speed images that were recorded for the main-post and single injection cases. The ensuing contour plots, which are also known as Intensity-aXial-Time (IXT) plots in the literature,[5] are presented in Fig. 7 and are used to derive key combustion characteristics of the injection cases, including ignition location, ignition delay, flame lift-off length, flame penetration distance and internal flame structure information. It is noted that ignition location is defined here as the distance from the nozzle where the flame luminosity is first detected. The ignition delay time, on the other hand, is defined as the elapsed time after the start of injection (aSOI), until the first detection of flame luminosity. The flame lift-off length and flame penetration distance refer to the average quasi-steady distances of the flame base and flame tip from the injector nozzle, respectively.

In Fig. 7, for the main-post injection cases, the two 'islands' on the plots represent the main (larger) and post (smaller) injection events. From the figure, it can be seen that whilst the overall shape of the islands on the contour plots are similar, some differences in the flame penetration, start of ignition, ignition location and intensity distribution characteristics can be observed for the post injections. In Fig. 7, the maximum flame penetration distances of the post injections are found be lower than their corresponding main injections, and the single injection reference case. This may be partly due to interactions between the fresh fuel from post injection with the combustion products from the main pulse. In addition, recent work[36,37] have also demonstrated that the strong enhancement in entrainment that occurs after the end of injection can interact with the fuel jet, causing the fuel vapor velocity and hence, penetration to fall below its steady-state value. Together, these can prevent the post injection flames from reaching their maximum quasi-steady state development. From

Fig. 7, it can also be observed that both the ignition locations and the flame lift-off lengths of the post injections are lower than their main injections and the single injection reference case. The ignition and lift-off distances of the injections, nevertheless, are still found to be greater than the maximum liquid penetration lengths observed in Fig. 6. These findings therefore indicate that there is no interaction between the spray and combustion processes under the test conditions of this work. When comparing the intensity distributions within the contour plots in Fig. 7, the peak luminosity values for both the main and post injection combustion events are found to be similar for all DTs. The post injections, however, are found to have marginally smaller areas with higher intensity, with the smallest area observed for the shortest DT (*i.e.*, 1.5 ms).

To further understand the changes in the ignition and combustion characteristics of the post injection events, the ignition delays, ignition locations and the flame lift-off lengths of the post injections, which are derived from the corresponding IXT plots in Fig. 7, are also plotted against the average values of their main injections in Fig. 8. Dashed lines through the data are used to help the visualization of the trends. Error bars (1 standard deviation) are also included to show the uncertainty associated with each data point. It is evident that the ignition delay, ignition location and flame lift-off length values of the post injections are shorter than that of the main injections. In addition, there is also a clear trend of shortening ignition delays and ignition locations with decreasing DT, whilst the flame lift-off lengths appear to reach an asymptote with longer DT. Previous studies[38,39] have reported that changes in ignition delay can impact on the time available for fuel-air mixing. This will directly affect the heat release profiles of the premixed and the mixing-controlled combustion processes, which in turn, will change the soot and temperature distribution of the flame.[5] Given that natural luminosity of a sooty flame is mainly comprised of hot soot incandescence,[40] which is a function of the local soot concentration and temperature,[41] the observed changes in the intensity distributions in the IXT plots (Fig. 7) with varied DTs can therefore be expected. In a previous study by Cung *et al.*,[5] it was noted that when sufficiently short DT is used, the combined momentum of the closely-coupled injections can push the ignition location and flame lift-off length of the later injection downstream from the nozzle. A near linear correlation between the changes in the ignition delays and ignition locations, in addition to a relatively invariant lift-off lengths of the flames across the varied DTs, however, is observed here. These trends imply that for the test conditions of this work, the DTs used were sufficiently long such that the momentum from the main injections have adequately decayed. From the time-sequenced flame luminosity images for the main-post injection with DT=1.5 ms (Fig. 2), it can be seen that whilst the combustion of the post injection was progressing towards the tail of the main injection, the combustion events were sufficiently separated. This observation is also reflected in the IXT plots presented in Fig. 8. From the figure, in the case of DT=1.5 ms, it can be seen that whilst the combustion of the post injection initiated when the main injection was still active, the contours associated with the two injection events are distinguishable. When the DT is longer, as in the cases of DT=2.0 and 2.5 ms, it can be also inferred from the IXT plots in Fig. 7 that the post combustion events only started after the main injections have extinguished. The consistently shorter flame lift-off lengths of the post injection flames, when compared with those of the main injection flames, also indicates that the injection duration specified for the post injection was not sufficiently long for the flames to revert back to their natural lift-off distances. It should also be noted that from Fig. 7, there is no indication of combustion ignition occurring upstream of the lift-off location (*i.e.*, combustion recession[42]) after the end of injection of the main, for all main-post injection cases.

To further understand the changes in the ignition and combustion characteristics of the post injection events, the IXT plots for the main-post injection cases, when subjected to a increased temperature ambient (1100 K) that is known to increase soot formation,[25] are also generated and plotted in Fig. 9. From the figure, it can be seen that the general features of the IXT plots are similar to that derived for the main-post injection cases in Fig. 7. It is noted, however, in contrast with the IXT plots in Fig. 7, the intensity distributions of the contour plots for the post injection events are found to be similar for all DTs. In addition, the flame luminosity signals for both the main and post injections are also found to recess back towards the injector, after their end of injections for all DTs – a phenomenon that was not observed at 900 K. This is consistent with the findings of previous studies,[42] which observed that lifted flame would have a greater propensity to propagate backwards towards the injector after its end of injection under high-temperature CI operating conditions. From the IXT plots, it can also be seen that the contours associated with the two injection events are distinguishable for all DTs, which indicate that the main and post injection combustion events were sufficiently separated at a higher ambient gas condition of 1100 K.

To provide a more quantitative assessment, the ignition delays, ignition locations and the flame lift-off lengths of the post injections, as derived from their corresponding IXT plots, are also plotted against the average values of their main injections, as shown in Fig. 10. When comparing the plots in Figs. 8 and 10, it can be seen at 1100 K, the ignition delay and location values of the post injections are also shorter than that measured for the main injections. The variations in the ignition delays and ignition locations of the post injections across the varied DT range, however, are within measurement uncertainties. The flame lift-off lengths of the post injection flames also appear unchanged and are of comparable values to their main injections, across the DT range. As is noted in previous studies,[20] an increase in ambient gas temperature would result in reduced lift-off length. The soot processes of the flame would therefore initiate at a distance that is closer to its nozzle, where the momentum effects of the main injections, if present, are expected to be more significant. The relatively trends in ignition parameters of the post injection flames therefore support the previous assertion that the DTs used were sufficiently long so that the momentum from the main injections have decayed. The similarity in the flame lift-off length values between the main and post injection combustion events, on the other hand, implies that the earlier ignition that occurred because of the higher ambient gas temperature, may have provided the post injection flames with sufficient time to stabilize at their natural lift-off distances before their end of injections. Together, one can therefore anticipate the ensuing the soot and temperature distribution, and hence, the natural luminosity of the post injection flames, to be similar across the DT range, as is observed in their IXT plots (Fig. 9).

4.3 Soot temperature and KL images

As is noted in the previous section and other studies,[40,41] the natural luminosity of a flame is a function of the local soot concentration and temperature. To gain further understanding of the interaction between the main and post injections, the soot temperature and KL distributions of the main and post injections at two ends of the investigated DT range (*i.e.*, DTs=1.5 and 2.5 ms) are generated, as presented in Figs. 12 and 13.

In the case of DT=1.5 ms, the soot temperature and KL distributions of the main and post injections are compared at three selected timing pairs of t_1=0.4 ms vs t_2=4.7 ms, t_1=0.6 ms vs t_2=4.9 ms and t_1=0.8 ms vs t_2=5.1 ms, as are shown in Fig. 12. The t_1 and t_2 correspond to the time after start of injection, for the main and post injections, respectively. The temporal positioning of these image pairs in the context of their injection rate profiles are shown in Fig. 11. It can be seen that the timing pairs are selected from the quasi-steady injection period to minimize the effects of the transient behaviors of the injection at the start and end of injections on the current findings. A shift of 4.3 ms between the two injections is selected, to ensure that the same amount of fuel has been injected for the main and post injections, at the three selected timing pairs.

Figure 12 presents the soot temperature and KL distributions for the main-post injection case, at three selected timing pairs. To facilitate direct, qualitative comparison, the soot temperature and KL images are divided into two, with the main and post injections presented at the left and right halves, respectively. The same scaling is also adopted for all time instants to facilitate qualitative comparison. For the soot temperature and KL images that are generated for the first timing pairs, it can be seen for the post injection event at t_2=4.7 ms, soot region is detectable at an axial distance of ∼20 mm and is found to extend to an axial distance of ∼28 mm from the injector nozzle. No two-color data, however, is observed at t_1=0.4 ms. However, for the images that are produced for the second timing pairs, it can be seen that the soot region becomes detectable for both the main and post injections, at an axial distance of ∼24 mm from nozzle. The soot region of the post injection at t_2=4.9 ms is observed to extend to an axial location of ∼41 mm, which is more downstream than that measured for main injection at t_1=0.6 ms (∼31 mm). For the third timing pairs, the same trends are observed to persist. The soot regions of both main and post injections at t_1=0.8 ms and t_2=5.1 ms are observable at similar axial distances from nozzle (∼25 mm). The span of the soot region of the post injection at t_2=5.1 ms (∼48 mm) is also found to be longer than that of the main injection at t_1=0.8 ms (∼38 mm). It should be noted that the soot region that is observable in the downstream region of the post injection at all three timings are from the main injection event, which was still active, during the initiation of the combustion of the post injection.

In the case of DT=2.5 ms, the soot temperature and KL distributions of the main and post injections are compared at three timing pairs of t_1=0.4 ms vs t_2=5.7 ms, t_1=0.6 ms vs t_2=5.9 ms and t_1=0.8 ms vs t_2=6.1 ms, and are presented in Fig. 13. The temporal positioning of these image pairs in the context of their injection rate profiles are also shown in Fig. 11. In this case, a shift of 5.3 ms between the two injections is selected to ensure the same amount of injected fuel at the three selected timing pairs. For the first timing pairs (t_1=0.4 ms and t_2=5.7 ms), it can be seen that soot region of the post injection is detectable at a distance of ∼20 mm from the nozzle. The image that is produced at t_1=0.4 ms, on the other hand, is found to only contain a few data points above detection limit. For the images that are generated for the second and third timing pairs (t_1=0.6 ms vs t_2=5.9 ms and t_1=0.8 ms vs t_2=6.1 ms), the soot regions of both the main and post injection events are detectable at ∼20 mm from the nozzle. The soot regions of the post injections are also found to have longer radial and axial spans, when compared with that observed for the main injections at corresponding time aSOI.

From the soot temperature images that are produced for the post injection events in Figs. 12 and 13 at DT=1.5 and 2.5 ms, it can be seen that the flame temperature of higher values are, to some extent, more evenly distributed within the frontal regions than that observed for the main injection flames at the same timings. As has been noted previously, no direct flame interaction between the main and post injection flames is observed, and that the coupling between the injections are mainly attributed to the interactions between the post injections and the combustion products from the main injections. Therefore, the relatively uniform temperature distributions that are observed in the soot temperature images of the post injections, may have been caused by the remaining combustion products heating the frontal regions of the incoming post injections.[5]

For comparison, the soot temperature and KL distributions of the main and post injections at two ends of the investigated DT range, but at 1100 K, are also generated and presented in Figs. 14 and 15. Again, the soot temperature and KL distributions of the main and post injections are produced at same three selected timing pairs, and the same scaling is adopted for the images to ease comparison. When comparing the soot temperature and KL distributions of the main and post injections at both ambient temperatures, and across the DT range, it can be seen that similar to the two-color images that were produced at 900 K, some discrepancies in the radial and axial spans of the main and post injection flames can be observed at 1100 K. However, in contrast to the two-color images at 900 K, the soot regions are already detectable for both the main and post injections, even at the first timing pairs. There is also little or no soot region that is observable in the downstream region of the post injection at all three timings, which indicate that there is no direct flame interaction between the main and post injection events, despite the more advanced ignition delays associated with the post injection flames at 1100 K. This is consistent with the observations made in the IXT plots of the main-post injections in Fig. 10. The relatively uniform temperature distributions across the jet that are observed for the soot temperature images of the post injections, however, are less apparent at 1100 K. This may be attributable to the optical uncertainty or limitation of the two-color method, which is discussed next.

4.4 Joint soot temperature and KL probability distributions

The temporal evolution of the spatially-averaged soot temperature and KL factor values of main and post injections at the two ends of the investigated DT range are also plotted in Fig. 16. For these plots, the average soot temperature and KL factor values are presented from the start of the soot emergence until the end of soot detection. From Fig. 16, it can be seen that the measured soot temperature and soot KL factor of the main and post injections increase rapidly to reach local peaks, before stabilizing at lower, quasi-steady values during the stabilized period of their injections. The average soot temperature and soot KL factor values of the main and post injection flames, however, are observed to increase after their end of injections, before the flames extinguished. It is noted that the measured values are sensitive to the experimental conditions and settings used. It is therefore challenging to perform a direct comparison of the current measurements with the results of previous studies. The observed values and the transient characteristics, at the start and end of injections, however, are broadly consistent to those measured for biodiesel flames under similar experimental settings by Zhang *et al.*[43] The exact reasons for the higher average soot temperature and soot KL factor, at the start and end of stabilized injection periods are unclear at present. However, it should be noted that the timings of the first local peaks are approximately coincident with the ignition delays of the flames, when the combustion processes can be expected to be transient. The accuracy of the two-color data recorded could therefore be affected by the presence of spatial gradients in soot properties across the flames at these time instants. Previous studies[36,37] have reported greater entrainment of ambient gases into the jet after the end of injection, which can lead to changes in the soot formation and oxidation processes. The second local peaks, which are observed to occur after their end of injection timings, may therefore be attributable to enhanced soot oxidation in the low soot temperature and KL zones from greater ambient gas entrainment. This can result in the measured average values to be dominated by soot signals from regions of higher local temperature and soot concentration values. Numerical calculations were also performed for comparison with the measured temperature results. For this work, zero-dimensional calculations were performed for the auto ignition of stagnant adiabatic homogeneous mixtures at initial ambient pressure and temperature values of 5.1 MPa and 900 K, respectively, with 15% oxygen concentration. A skeletal mechanism with 115 species and 460 reactions[44] was used. It is noted previous studies[45,46] have reported that methyl decanoate/n-heptane mixtures are good surrogates for canola oil based biofuels, an equimolar blend of methyl decanoate and n-heptane as was therefore used as the biodiesel surrogate mixture for the calculations. The results of the numerical calculations reveal that a maximum temperature of 2200 K can be attained at the simulated ambient condition, which is lower than the maximum average temperature value of 2316 K that was experimentally observed during the quasi-steady period for the canola oil biodiesel. As is noted previously, the two-color results can significantly overestimate the actual flame temperature value and are biased towards the soot in the hottest flame surface that is located closest to the detector. In addition, there is also a difference in the higher heating values of methyl decanoate (*i.e.*, 36.7 MJ/kg) and canola oil biodiesel (*i.e.*, 38.1 MJ/kg).[23] All these factors contribute to the difference in measured temperature.

Joint probability density functions (PDFs) have been demonstrated to be useful in revealing statistical relationships between the variables of interest[47,48] and are used to provide a measure of the soot temperature and soot KL values occurring concurrently at the same point in time for the main and post injection events. The joint PDFs between the soot temperature and KL factor at the three selected timing pairs for both main-post injection cases are generated and presented in Figs. 17 and 18, with the pseudo color contour representing the probability of the data sets. From the PDFs, it can be seen that the spans and the average measured soot KL values decrease as the average measured soot temperature values increase. It is noted that the overall traits of the PDFs obtained are consistent with those of a soot temperature versus soot KL temperature correlation plot for an n-heptane flame, which was also measured using two-color pyrometry technique in a previous study.[31] In previous studies,[49] optical diagnostics have shown that diesel jet flame comprises of a relative cooler inner jet core that is surrounded by a thin diffusion flame, with soot occurring throughout the jet cross section. The two-color data obtained from a diffusion flame is therefore be more weighted towards the soot present in the hotter diffusion flame reaction zone, than in the flame core. In addition, as the temperature of the flame increases, the weight of the soot signal from the flame front would also increase in relation to the soot signal from the flame core, such that the two-color data would become more representative of the soot properties in the flame edge only. All these can contribute towards the lower measured soot KL and span at higher flame temperatures observed in the PDFs.

In the case of DT=1.5 ms, for the PDF pairs that are generated for the first time instants (t_1=0.4 ms and t_2=4.7 ms), it can be seen that no data point is detected at t_1=0.4 ms. This is to be expected, given the measured ignition delay of the flame is ∼0.6 ms (see Fig. 8) and therefore the combustion process has not commenced at this time instant. The measured soot temperature values at t_2=4.7 ms, on the other hand, are found to be distributed between 1900 K and 2500 K. From Fig. 8, it can be seen that at DT=1.5 ms, the measured ignition delay of the post injection is found to be ∼0.37 ms aSOI. Therefore, the combustion of the post injection would have initiated prior to the first time instant for which the image pairs is selected for comparison. Nonetheless, the observed trend at t_2=4.7 ms is mainly attributed to the burnout of the main injection, which is the dominant combustion event at this time instant. From the PDFs that are produced for the second and third timing pairs, it can be seen that the soot temperatures measured at t_2=4.9 ms and 5.1 ms, are distributed between 1900 K and 2700 K. These values are not only higher than the temperature of the main injection combustion events observed at t_1=0.6 ms and 0.8 ms (between 1600 K and 2380 K), but also higher than those of the combustion process of the main injection at t_2=4.7 ms. From Fig. 12, it can be seen that whilst the combustion of the main injection was still active at t_2=4.9 ms and 5.1 ms, the combustion regions that are associated with the main injection are small, and therefore do not significantly influence the overall shapes and trends of the PDFs at these time instants.

In the case of DT=2.5 ms, from the PDFs that are generated for the first timing pairs (t_1=0.4 ms and t_2=5.7 ms), it can be seen that no data point is again detected at t_1=0.4 ms. The data points for the PDF that is generated for t_2=5.7 ms, however, are observed to be relatively scattered. It is noted that at this time instant, which corresponds to 0.4 ms after the start of second injection, is approximately coincident with the measured ignition delay of the second injection. Given that the combustion process was still initiating, the images recorded would therefore only contain a low sample size of soot temperature and KL data. From the PDFs that are produced for the second and third timing pairs, it can be seen that the temperature values measured at t_2=5.9 ms and 6.1 ms, are distributed between 1900 K and 2650 K. The measured temperature values for the post injections are again found to be higher than that observed for the main injection combustion events at t_1=0.6 ms and 0.8 ms (between 1600 K and 2400 K). As is noted previously, the two-color pyrometry technique has significant temperature uncertainty and therefore the temperature values derived should only be used for qualitative comparison. Nonetheless, the overall trends of the PDFs are consistent in showing that combustion of the post injection events were occurring at higher temperature values. From the PDFs that are presented in Figs. 17 and 18, it can also be seen that the most probable soot KL factors of the post injection are generally observed to have narrower distributions and lower average values than that of the main.

For comparative measurements, the temporal evolution of the spatially-averaged soot temperature and KL factor values of main and post injections at an ambient temperature condition of 1100 K, are also plotted in Fig. 16. When comparing the plots in Figs. 16 and 19, it can be seen that the plots share similar overall characteristics, but the average soot temperature and soot concentration factor profiles of the main-post injection cases at 1100 K, are less transient at their start of injections and are observed to attain more stable quasi-steady values. As is discussed previously, the higher ambient temperature results in a shorter ignition delay, which can contribute towards the flame having more time to attain a quasi-steady state, prior to its end of injection. From Fig. 19, the average soot KL factors of the flames at 1100 K in Fig. 19 are observed to be approximately two times greater than the measured values at 900 K. As is noted in previous studies,[20] an increase in the ambient gas temperature can result in a shortening of the lift-off length, and hence, reduced amount of fuel-air premixing occurring upstream. This can cause the soot processes to initiate earlier and hence, the peak soot level of the flame to increase, as is observed in this work.

The joint PDFs for both main-post injection cases at the three selected timings are also presented in Figs. 20 and 21. From the figures, it can be seen that some trends in the joint PDFs are already observable, even for the images that were recorded for the first timing pairs. Given that all of the measured ignition delay of the flames are earlier than ∼0.27 ms (see Fig. 10), the combustion processes for the flames would have commenced to generate sufficient emission signals that can be used for two-color measurements at the first time instants (t_1=0.4 ms and t_2=4.7 ms). From the figures, it can be seen when DT=1.5 ms, the temperature values of the main injection at t_1=0.4 ms are distributed between 2000 and 2400 K, whereas the measured values for the post injection to span from 2000 to 2600 K at t_2=4.7 ms. The distributions and the average values of the PDFs for the main and post injections, however, are similar for the second and third timing pairs. In the case of DT=2.5 ms, the overall distributions and the average values of the PDFs for the main and post injections are alike for all three timing pairs. The general similarity in the distributions and average values observed for the post injections, across the varied DTs, implies that the changes in the soot temperature and concentration distributions of the post injections that arise from their interactions with the combustion products from the main pulse are within measurement uncertainty. This is consistent with the earlier observations of the relative invariant intensity distributions in the IXT plots of the post injection flames in Fig. 10. From the figures, it can be seen the most probable soot KL factors of the PDFs at 1100 K are distributed over a wider range of soot concentration values than that observed for the PDFs at 900 K. As is discussed previously, an increase in ambient gas temperature can enhance the soot formation process, and therefore the soot content of the flame. Nonetheless, previous studies[31] have also indicated that, as the temperature across the flame volume is increased, the measurement would become more and more influenced by the soot in both the flame region and jet core, therefore producing measurements that are higher, but more representative of the soot properties across the flame volume.

Together, the PDF results and the findings presented in the previous sections demonstrate that the ignition and combustion characteristics of the post injections are affected by their interactions with the combustion products from the main injections, over the tested DT range. The results indicate that the changes in soot temperature and concentration distributions are affected by the extent of the interactions between the injections, such that the post injection event with the shortest DT (*i.e.*, 1.5 ms) is found to ignite earlier with soot zone that developed more rapidly with higher temperature and soot concentration. It is presently unclear, however, if the higher flame temperature would result in more effective soot oxidation, or if the more rapid soot zone development would lead to increased engine-out soot emissions. It should be noted that the two-color data would become more biased towards the soot properties at the flame surface, because of the higher temperature values of the post injection combustion process, and this could also contribute towards the lower soot KL values observed. Further investigation, including using more quantitative soot concentration and temperature imaging techniques such as laser-induced incandescence (LII) and nonlinear two-line atomic fluorescence (NTLAF) methods,[50–53] is required to confirm the current trends qualitatively and to extend them to actual engine outputs.

5 Conclusion

An experiment was performed in an optically-accessible, constant-volume combustion chamber to evaluate the effects of varying dwell time (DT) between the main and post injections.

A compression-ignition (CI) engine environment with an ambient density, bulk temperature and oxygen concentration of 19.4 kg/m^3, 900 K and 15 vol.% O_2, respectively, were used. A mass ratio of the main to post injections of 80% to 20% was maintained for the main-post injections, but the DT between the injections were varied from 1.5 ms to 2.5 ms. A canola oil based biodiesel was used and the injection pressure of the fuel was fixed at 100 MPa. Comparative measurements were performed using the same fuel and injection schedules, but subjected to a higher ambient gas temperature condition of 1100 K. For this work, diffused-back illumination and high-speed flame luminosity imaging techniques were used to obtain liquid phase and combustion information of the test cases. The results indicated that under the test conditions of this work, the ignition delays, ignition locations and the flame lift-off lengths of the post injection flames were found to be consistently shorter than that of the main-flames. The differences in ignition delays and locations between the main and post injection flames, however, were found to reduce with increasing DT, which suggest that the observed modifications in the ignition and combustion behaviors of the post injections appeared to be driven by the extent of their interactions with the combustion products of the main flames. Two-color pyrometry technique was also used to provide soot temperature and soot KL information for the main-post injection cases. From the two-color data, it can be seen that the interaction between the main and post injections was found to cause the soot zones of the post injections to develop more rapidly, and at higher temperature values, after the ignition. The distribution of the most probable soot KL factors of the post injections were found to be narrower, and have lower soot content values. Further studies, however, are required to validate the observed soot concentration trends.

Acknowledgement

The authors acknowledge the financial support of Australian Research Council (ARC) and an Australian Academy of Technological Sciences and Engineering (ATSE) Priming Grant. The authors also acknowledge the contributions of Cheng Wang, Matt Mills and Brad Moody.

References

(1) Knecht, W. Some historical steps in the development of the common rail injection system. *Transactions of the Newcomen Society* **2004**, *74*, 89–107.

(2) Felsch, C.; Gauding, M.; Hasse, C.; Vogel, S.; Peters, N. An extended flamelet model for multiple injections in DI Diesel engines. *Proceedings of the Combustion Institute* **2009**, *32*, 2775 – 2783.

(3) Bolla, M.; Chishty, M. A.; Hawkes, E. R.; Kook, S. Modeling combustion under engine combustion network Spray A conditions with multiple injections using the transported probability density function method. *International Journal of Engine Research* **2017**, *18*, 6–14.

(4) O'Connor, J.; Musculus, M. Effects of exhaust gas recirculation and load on soot in a heavy-duty optical diesel engine with close-coupled post injections for high-efficiency combustion phasing. *International Journal of Engine Research* **2014**, *15*, 421–443.

(5) Cung, K.; Moiz, A.; Johnson, J.; Lee, S.-Y.; Kweon, C.-B.; Montanaro, A. Spray-combustion interaction mechanism of multiple-injection under diesel engine conditions. *Proceedings of the Combustion Institute* **2015**, *35*, 3061–3068.

(6) Kim, M. Y.; Yoon, S. H.; Park, K. H.; Lee, C. S. Effect of multiple injection strategies on the emission characteristics of Dimethyl Ether (DME)-fueled compression ignition engine. *Energy & Fuels* **2007**, *21*, 2673–2681.

(7) Lee, J. Experimental investigation of thermal load in high speed direct injection diesel engine under the control of various engine performance parameters. *Journal of Engineering for Gas Turbines and Power* **2011**, *133*, 032802–032802–8.

(8) Park, S. H.; Yoon, S. H.; Lee, C. S. Effects of multiple-injection strategies on overall spray behavior, combustion, and emissions reduction characteristics of biodiesel fuel. *Applied Energy* **2011**, *88*, 88–98.

(9) O'Connor, J.; Musculus, M. Post injections for soot reduction in diesel engines: A review of current understanding. *SAE International Journal of Engines* **2013**, *6*, 400–421.

(10) Jeftić, M.; Zheng, M. A study of the effect of post injection on combustion and emissions with premixing enhanced fueling strategies. *Applied Energy* **2015**, *157*, 861 – 870.

(11) Bobba, M.; Musculus, M.; Neel, W. Effect of post injections on in-cylinder and exhaust soot for low-temperature combustion in a heavy-duty diesel engine. *SAE International Journal of Engines* **2010**, *3*, 496–516.

(12) Sperl, A. The influence of post-injection strategies on the emissions of soot and particulate matter in heavy duty Euro V diesel engine. *SAE Paper* **2011**, 2011–36–0350.

(13) Mancaruso, E.; Merola, S. S.; Vaglieco, B. M. Study of the multi-injection combustion process in a transparent direct injection common rail diesel engine by means of optical techniques. *International Journal of Engine Research* **2008**, *9*, 483–498.

(14) Desantes, J.; Arrègle, J.; López, J.; García, A. A comprehensive study of diesel combustion and emissions with post-injection. *SAE Paper* **2007**, 2007–01–0915.

(15) Han, Z.; Uludogan, A.; Hampson, G.; Reitz, R. Mechanism of soot and NOx emission reduction Using multiple-injection in a diesel engine. *SAE Paper* **1996**, 960633.

(16) Zhang, Y.; Boehman, A. L. Impact of biodiesel on NO_x emissions in a common rail direct injection diesel engine. *Energy & Fuels* **2007**, *21*, 2003–2012.

(17) Jing, W.; Wu, Z.; Roberts, W. L.; Fang, T. Spray combustion of biomass-based renewable diesel fuel using multiple injection strategy in a constant volume combustion chamber. *Fuel* **2016**, *181*, 718–728.

(18) Chuck, C. J.; Bannister, C. D.; Hawley, J. G.; Davidson, M. G.; Bruna, I. L.; Paine, A. Predictive model to assess the molecular structure of biodiesel fuel. *Energy & Fuels* **2009**, *23*, 2290–2294.

(19) Kuti, O. A.; Zhu, J.; Nishida, K.; Wang, X.; Huang, Z. Characterization of spray and combustion processes of biodiesel fuel injected by diesel engine common rail system. *Fuel* **2013**, *104*, 838–846.

(20) Pickett, L. M.; Siebers, D. L. Soot in diesel fuel jets: effects of ambient temperature, ambient density, and injection pressure. *Combustion and Flame* **2004**, *138*, 114–135.

(21) Meijer, M.; Somers, B.; Johnson, J.; Naber, J.; Lee, S.-Y.; Malbec, L. M. C.; Bruneaux, G.; Pickett, L. M.; Bardi, M.; Payri, R.; Bazyn, T. Engine combustion network (ECN): characterization and comparison of boundary conditions for different combustion vessels. *Atomization and Sprays* **2012**, *22*, 777–806.

(22) Pickett, L. M.; López, J. J. Jet-wall interaction effects on diesel combustion and soot formation. *SAE paper* **2005**, 2005–01–0921.

(23) Pham, X. P. Influences of molecular profiles of biodiesels on atomization, combustion and emission characteristics. Ph.D. thesis, School of Aerospace, Mechanical and Mechatronic Engineering, The University of Sydney, 2015.

(24) Ming, C.; Fattah, I. R.; Chan, Q. N.; Pham, P. X.; Medwell, P. R.; Kook, S.; Yeoh, G. H.; Hawkes, E. R.; Masri, A. R. Combustion characterization of waste cooking oil and canola oil based biodiesels under simulated engine conditions. *Fuel* **2018**, *224*, 167 – 177.

(25) Kook, S.; Pickett, L. M. Soot volume fraction and morphology of conventional, Fischer-Tropsch, coal-derived, and surrogate fuel at diesel conditions. *SAE International Journal of Fuels and Lubricants* **2012**, *5*, 647–664.

(26) Pham, P.; Bodisco, T.; Stevanovic, S.; Rahman, M.; Wang, H.; Ristovski, Z.; Brown, R.; Masri, A. Engine performance characteristics for biodiesels of different degrees of saturation and carbon chain lengths. *SAE International Journal of Fuels and Lubricants* *6*, 188–198.

(27) Pham, P. X.; Bodisco, T. A.; Ristovski, Z. D.; Brown, R. J.; Masri, A. R. The influence of fatty acid methyl ester profiles on inter-cycle variability in a heavy duty compression ignition engine. *Fuel* **2014**, *116*, 140–150.

(28) Siebers, D. Liquid-phase fuel penetration in diesel sprays. *SAE paper* **1998**, 980809.

(29) Pickett, L. M.; Genzale, C. L.; Manin, J. Uncertainty quatification for liquid penetration of evaporating sprays at diesel-like conditions. *Atomization and Sprays* **2015**, *25*, 425–452.

(30) Larsson, A. Optical studies in a DI diesel engine. *SAE paper* **1999**, 1999–01–3650.

(31) Svensson, K. I.; Mackrory, A. J.; Richards, M. J.; Tree, D. R. Calibration of an RGB, CCD camera and interpretation of its two-color images for KL and temperature. *SAE paper* **2005**, 2005–01–0648.

(32) Zha, K.; Florea, R.-C.; Jansons, M. Soot evolution with cyclic crank-angle-resolved two-color thermometry in an optical diesel engine fueled with biodiesel blend and ULSD. *Journal of Engineering for Gas Turbines and Power* **2012**, *134*, 092803–092803–7.

(33) Wang, X.; Huang, Z.; Zhang, W.; Kuti, O. A.; Nishida, K. Effects of ultra-high injection pressure and micro-hole nozzle on flame structure and soot formation of impinging diesel spray. *Applied Energy* **2011**, *88*, 1620–1628.

(34) Musculus, M. P. B.; Singh, S.; Reitz, R. D. Gradient effects on two-color soot optical pyrometry in a heavy-duty DI diesel engine. *Combustion and Flame* **2008**, *153*, 216–227.

(35) Pickett, L. M.; Kook, S.; Williams, T. Transient liquid penetration of early-injection diesel sprays. *SAE International Journal of Engines* **2009**, *2*, 785–804.

(36) Musculus, M.; Lachaux, T.; Pickett, L.; Idicheria, C. End-of-injection over-mixing and unburned hydrocarbon emissions in low-temperature-combustion diesel engines. *SAE paper* **2007**, 2007–01–0907.

(37) Musculus, M.; Kattke, K. Entrainment waves in diesel jets. *SAE paper* **2009**, 2009–01–1355.

(38) Higgins, B.; Siebers, D. L.; Aradi, A. Diesel-spray ignition and premixed-burn behavior. *SAE paper* **2000**, 2000–01–0940.

(39) Liu, H.; Lee, C.-f. F.; Huo, M.; Yao, M. Combustion characteristics and soot distributions of neat butanol and neat soybean biodiesel. *Energy & Fuels* **2011**, *25*, 3192–3203.

(40) Wang, X.; Kuti, O. A.; Zhang, W.; Nishida, K.; Huang, Z. Effect of injection pressure on flame and soot characteristics of the biodiesel fuel spray. *Combustion Science and Technology* **2010**, *182*, 1369–1390.

(41) Zhao, H.; Ladommatos, N. Optical diagnostics for soot and temperature measurements in diesel engines. *Progress in Energy and Combustion Science* **1998**, *24*, 221–255.

(42) Knox, B. W.; Genzale, C. L.; Pickett, L. M.; García-Oliver, J. M. Combustion recession after end of injection in diesel sprays. *SAE International Journal of Engines* **2015**, *8*, 679–695.

(43) Zhang, J.; Jing, W.; Roberts, W. L.; Fang, T. Soot measurements for diesel and

biodiesel spray combustion under high temperature highly diluted ambient conditions. *Fuel* **2014**, *135*, 340–351.

(44) Luo, Z.; Plomer, M.; Lu, T.; Som, S.; Longman, D. E.; Sarathy, S.; Pitz, W. J. A reduced mechanism for biodiesel surrogates for compression ignition engine applications. *Fuel* **2012**, *99*, 143–153.

(45) Lele, A. D.; Anand, K.; Narayanaswamy, K. In *Biofuels: Technology, Challenges and Prospects*; Agarwal, A. K., Agarwal, R. A., Gupta, T., Gurjar, B. R., Eds.; Springer Singapore: Singapore, 2017; pp 177–199.

(46) Herbinet, O.; Pitz, W. J.; Westbrook, C. K. Detailed chemical kinetic mechanism for the oxidation of biodiesel fuels blend surrogate. *Combustion and Flame* **2010**, *157*, 893–908.

(47) Chan, Q. N.; Medwell, P. R.; Nathan, G. J. Algorithm for soot sheet quantification in a piloted turbulent jet non-premixed natural gas flame. *Experiments in Fluids* **2014**, *55*, 1827.

(48) Gu, D.; Sun, Z.; Dally, B. B.; Medwell, P. R.; Alwahabi, Z. T.; Nathan, G. J. Simultaneous measurements of gas temperature, soot volume fraction and primary particle diameter in a sooting lifted turbulent ethylene/air non-premixed flame. *Combustion and Flame* **2017**, *179*, 33–50.

(49) Dec, J. E. A conceptual model of DI diesel combustion based on laser-sheet imaging. *SAE paper* **1997**, 970873.

(50) Chan, Q. N.; Medwell, P. R.; Kalt, P. A. M.; Alwahabi, Z. T.; Dally, B. B.; Nathan, G. J. Simultaneous imaging of temperature and soot volume fraction. *Proceedings of the Combustion Institute* **2011**, *33*, 791–798.

(51) Chan, Q. N.; Medwell, P. R.; Alwahabi, Z. T.; Dally, B. B.; Nathan, G. J. Assessment of interferences to nonlinear two-line atomic fluorescence (NTLAF) in sooty flames. *Applied Physics B* **2011**, *104*, 189–198.

(52) Medwell, P. R.; Chan, Q. N.; Dally, B. B.; Mahmoud, S.; Alwahabi, Z. T.; Nathan, G. J. Temperature measurements in turbulent non-premixed flames by two-line atomic fluorescence. *Proceedings of the Combustion Institute* **2013**, *34*, 3619–3627.

(53) Qamar, N. H.; Alwahabi, Z. T.; Nathan, G. J.; Chan, Q. N. Soot sheet dimensions in turbulent nonpremixed flames. *Combustion and Flame* **2011**, *158*, 2458–2464.

Table 1: Summary of test conditions, fuel composition, properties and injection conditions.

Test conditions	
Ambient density (kg/m^3)	19.4
Ambient pressure (MPa)	5.1, 6
Bulk temperature at injection (K)	900, 1100
Oxygen level (vol.%)	0 (non-reacting), 15 (reacting)
Fuel fatty acid profiles (wt%)	
Palmitic, C16:0	4.3
Stearic, C18:0	2.2
Oleic, C18:1	63.5
Linoleic, C18:2	18.9
Linolenic, C18:3	9.2
Eicosanoic, C20:0	0.4
Eicosenoic, C20:1	1.1
Fuel properties	
Fuel abbreviation	C1875
Oxygen content (wt%)	10.83
Iodine number	105
Saponification number	185
Cetane number	59
Fuel injection conditions	
Nozzle diameter (µm)	105
Injection pressure (MPa)	100
Injection quantity (mg)	10 (single) 8:2 (main-post)
Injection duration (ms)	4.87 (single) 3.8:1 (main-post)
Dwell time (ms)	Single, 1.5, 2.0 and 2.5

List of Figures

1 Schematic diagram of the experimental arrangement, including the combustion chamber and high-speed flame luminosity imaging setup. 36

2 Typical time-sequenced flame luminosity images for a main-post injection case, with a dwell time (DT) of 1.5 ms. The fuel is injected from left to right in this these images. 37

3 Schematic diagram of the experimental arrangement, including the combustion chamber and diffused back illumination and Mie-scattering imaging setup. 38

4 Normalized optical response of the red, green and blue channels of the high-speed camera used. 39

5 Soot temperature (top) and soot KL (bottom) surfaces in the domain of red and green signal intensity values, expressed in arbitrary units. 40

6 Liquid penetration profiles, as a function of time after start of injection (aSOI), for the main-post and single injection cases. The dwell times of the profiles are also indicated on the plot. 41

7 Average Intensity-aXial-Time (IXT) plots for the main-post and single injection cases. The start of injection timings and ignition delays of the post injections are indicated with dashed lines. Ambient temperature: 900 K. Fuel: Canola oil biodiesel. 42

8 Ignition delay, ignition location and average flame lift-off length values of the main and post injection events for the main-post injection cases with dwell times (DTs) of 1.5, 2.0 and 2.5 ms. Ambient temperature: 900 K. 43

9 Average Intensity-aXial-Time (IXT) plots for the main-post cases. The start of injection timings and ignition delays of the post injections are indicated with ashed lines. Ambient temperature: 1100 K. 44

10 Ignition delay, ignition location and average flame lift-off length values of the main and post injection events for the main-post injection cases with dwell times (DTs) of 1.5, 2.0 and 2.5 ms. Ambient temperature: 1100 K. 45

11 Injection rate profiles for the main-post injection cases, with a fixed fuel mass ratio of main to post injections of 80% to 20%, but with varied dwell times (DTs) of 1.5 ms (top) and 2.5 ms (bottom). t_1 and t_2 represent selected time instants after the start of injection, for the main and post injections, respectively. For DT=1.5 ms (top), the two-color data for the main and post injections are compared at three selected timing pairs of t_1=0.4 ms vs t_2=4.7 ms, t_1=0.6 ms vs t_2=4.9 ms and t_1=0.8 ms vs t_2=5.1 ms, respectively. For DT=2.5 ms (bottom), the two-color data for the main and post injections are compared at three selected timing pairs of t_1=0.4 ms vs t_2=5.7 ms, t_1=0.6 ms vs t_2=5.9 ms and t_1=0.8 ms vs t_2=6.1 ms, respectively. 46

12 Comparisons of spatial distributions of typical, instantaneous soot temperature and soot KL of the main (left half) and post injections (right half), at three selected timing pairs, for the main-post case with a dwell time (DT) of 1.5 ms. The fuel is injected from the top to bottom, in these images. Ambient temperature: 900 K. 47

13 Comparisons of spatial distributions of typical, instantaneous soot temperature and soot KL of the main (left half) and post injections (right half), at three selected timing pairs, for the main-post case with a dwell time (DT) of 2.5 ms. The fuel is injected from the top to bottom, in these images. Ambient temperature: 900 K. 48
14 Comparisons of spatial distributions of typical, instantaneous soot temperature and soot KL of the main (left half) and post injections (right half), at three selected timing pairs, for the main-post case with a dwell time (DT) of 1.5 ms. The fuel is injected from the top to bottom, in these images. Ambient temperature: 1100 K. 49
15 Comparisons of spatial distributions of typical, instantaneous soot temperature and soot KL of the main (left half) and post injections (right half), at three selected timing pairs, for the main-post case with a dwell time (DT) of 2.5 ms. The fuel is injected from the top to bottom, in these images. Ambient temperature: 1100 K. 50
16 The time-resolved results for spatially-averaged soot two-color temperature (upper) and soot KL factor values (lower) for the main-post injection cases with dwell times (DTs) of 1.5 and 2.5 ms, respectively. The start of injection and end of injection timings for the main-post injection cases are indicated on the plots using dashed lines. Ambient temperature: 900 K. 51
17 Comparisons of joint PDFs of soot temperature and soot KL of the main (left) and post (right) injections at three selected time steps, for a main-post injection case with a dwell time (DT) of 1.5 ms. All time instants have the same color scale. Ambient temperature: 900 K. 52
18 Comparisons of joint PDFs of soot temperature and soot KL of the main (left) and post (right) injections at three selected time steps, for a main-post injection case with a dwell time (DT) of 2.5 ms. All time instants have the same color scale. Ambient temperature: 900 K. 53
19 The time-resolved results for spatially-averaged soot two-color temperature (upper) and soot KL factor values (lower) for the main-post injection cases with dwell times (DTs) of 1.5 and 2.5 ms, respectively. The start of injection and end of injection timings for the main-post injection cases are indicated on the plots using dashed lines. Ambient temperature: 1100 K. 54
20 Comparisons of joint PDFs of soot temperature and soot KL of the main (left) and post (right) injections at three selected time steps, for a main-post injection case with a dwell time (DT) of 1.5 ms. All time instants have the same color scale. Ambient temperature: 1100 K. 55
21 Comparisons of joint PDFs of soot temperature and soot KL of the main (left) and post (right) injections at three selected time steps, for a main-post injection case with a dwell time (DT) of 2.5 ms. All time instants have the same color scale. Ambient temperature: 1100 K. 56

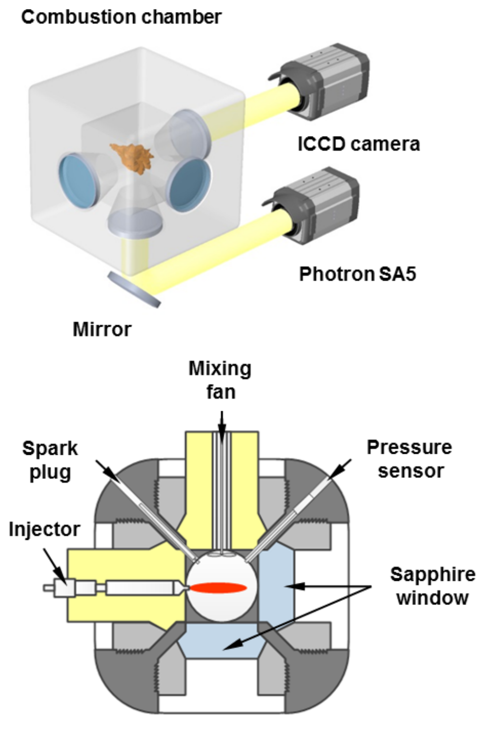

Figure 1: Schematic diagram of the experimental arrangement, including the combustion chamber and high-speed flame luminosity imaging setup.

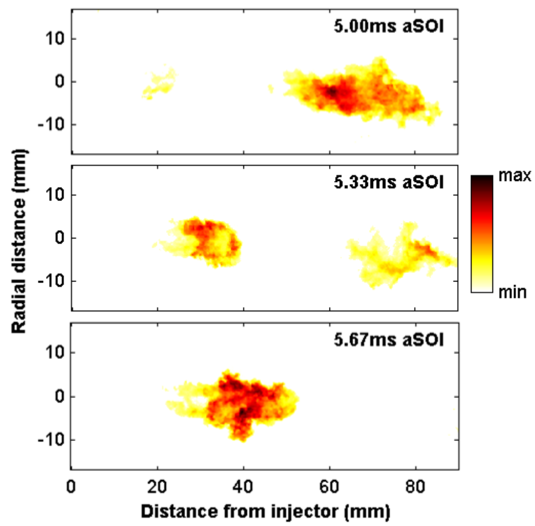

Figure 2: Typical time-sequenced flame luminosity images for a main-post injection case, with a dwell time (DT) of 1.5 ms. The fuel is injected from left to right in this these images.

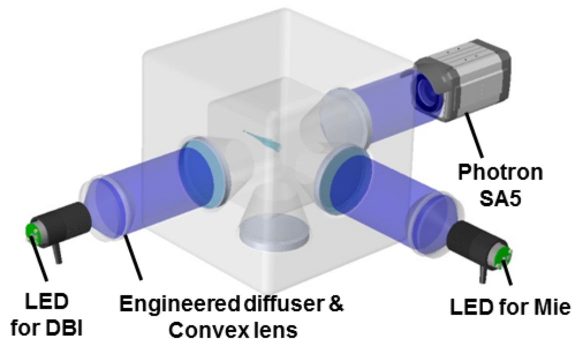

Figure 3: Schematic diagram of the experimental arrangement, including the combustion chamber and diffused back illumination and Mie-scattering imaging setup.

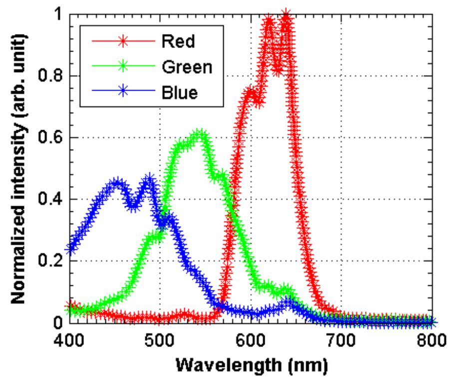

Figure 4: Normalized optical response of the red, green and blue channels of the high-speed camera used.

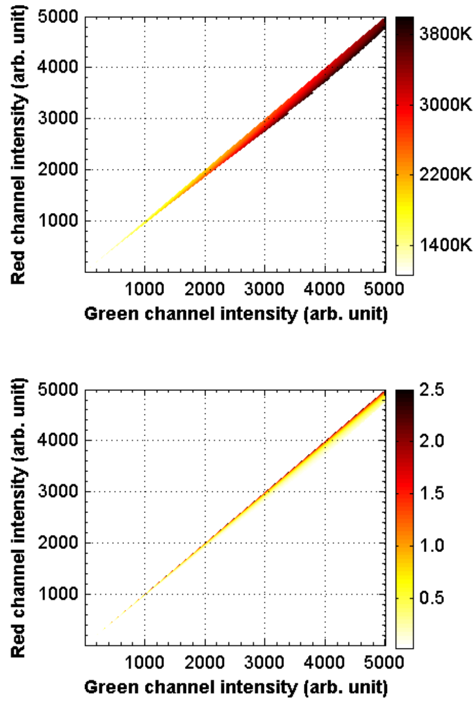

Figure 5: Soot temperature (top) and soot KL (bottom) surfaces in the domain of red and green signal intensity values, expressed in arbitrary units.

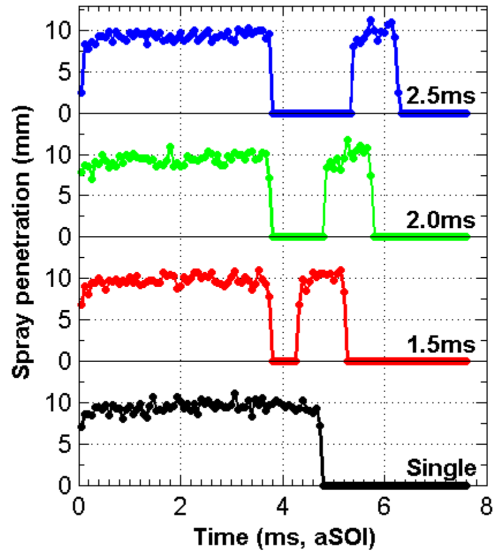

Figure 6: Liquid penetration profiles, as a function of time after start of injection (aSOI), for the main-post and single injection cases. The dwell times of the profiles are also indicated on the plot.

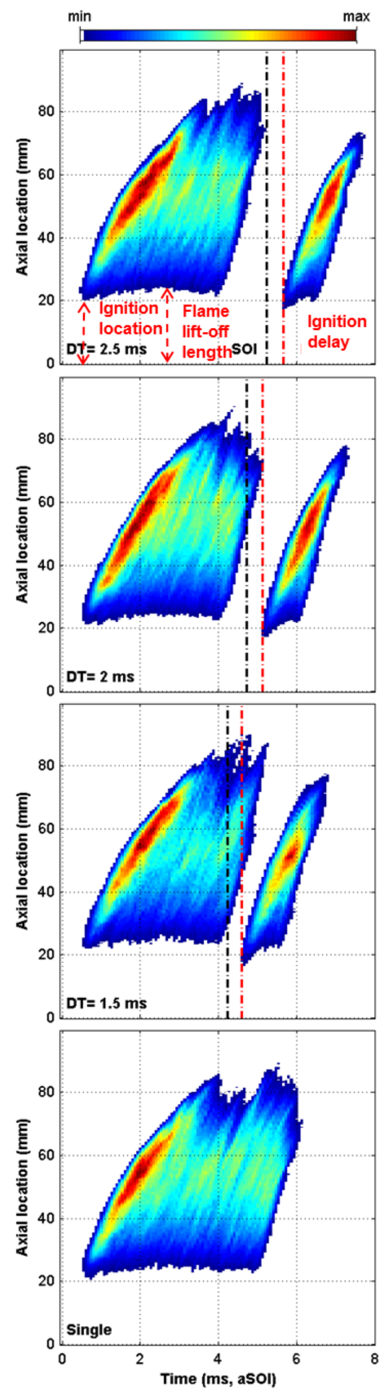

Figure 7: Average Intensity-aXial-Time (IXT) plots for the main-post and single injection cases. The start of injection timings and ignition delays of the post injections are indicated with dashed lines. Ambient temperature: 900 K. Fuel: Canola oil biodiesel.

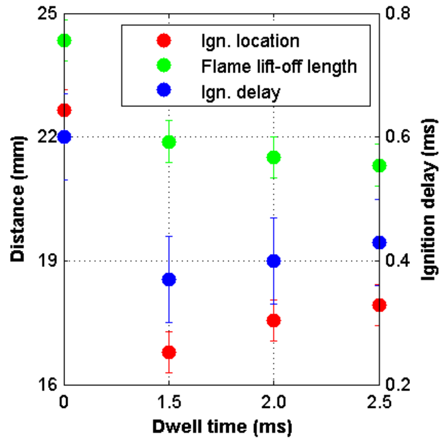

Figure 8: Ignition delay, ignition location and average flame lift-off length values of the main and post injection events for the main-post injection cases with dwell times (DTs) of 1.5, 2.0 and 2.5 ms. Ambient temperature: 900 K.

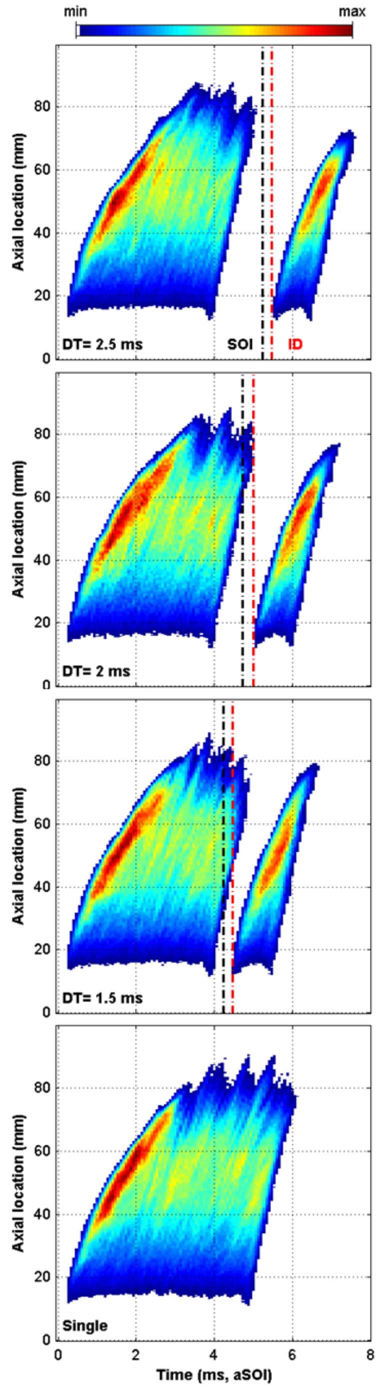

Figure 9: Average Intensity-aXial-Time (IXT) plots for the main-post cases. The start of injection timings and ignition delays of the post injections are indicated with ashed lines. Ambient temperature: 1100 K.

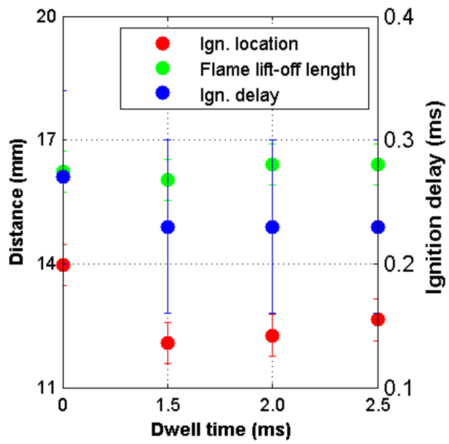

Figure 10: Ignition delay, ignition location and average flame lift-off length values of the main and post injection events for the main-post injection cases with dwell times (DTs) of 1.5, 2.0 and 2.5 ms. Ambient temperature: 1100 K.

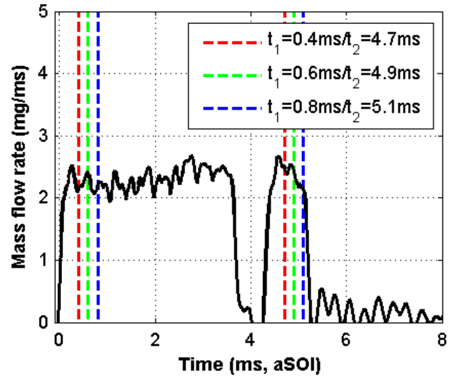

Figure 11: Injection rate profiles for the main-post injection cases, with a fixed fuel mass ratio of main to post injections of 80% to 20%, but with varied dwell times (DTs) of 1.5 ms (top) and 2.5 ms (bottom). t_1 and t_2 represent selected time instants after the start of injection, for the main and post injections, respectively. For DT=1.5 ms (top), the two-color data for the main and post injections are compared at three selected timing pairs of t_1=0.4 ms vs t_2=4.7 ms, t_1=0.6 ms vs t_2=4.9 ms and t_1=0.8 ms vs t_2=5.1 ms, respectively. For DT=2.5 ms (bottom), the two-color data for the main and post injections are compared at three selected timing pairs of t_1=0.4 ms vs t_2=5.7 ms, t_1=0.6 ms vs t_2=5.9 ms and t_1=0.8 ms vs t_2=6.1 ms, respectively.

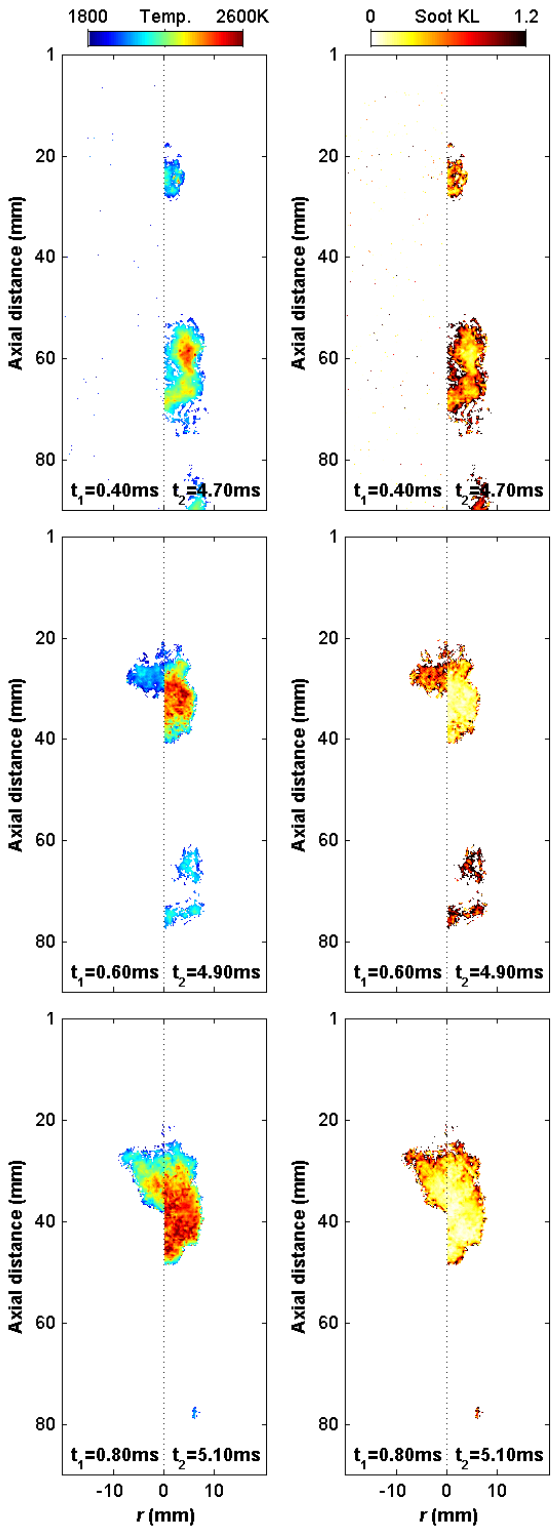

Figure 12: Comparisons of spatial distributions of typical, instantaneous soot temperature and soot KL of the main (left half) and post injections (right half), at three selected timing pairs, for the main-post case with a dwell time (DT) of 1.5 ms. The fuel is injected from the top to bottom, in these images. Ambient temperature: 900 K.

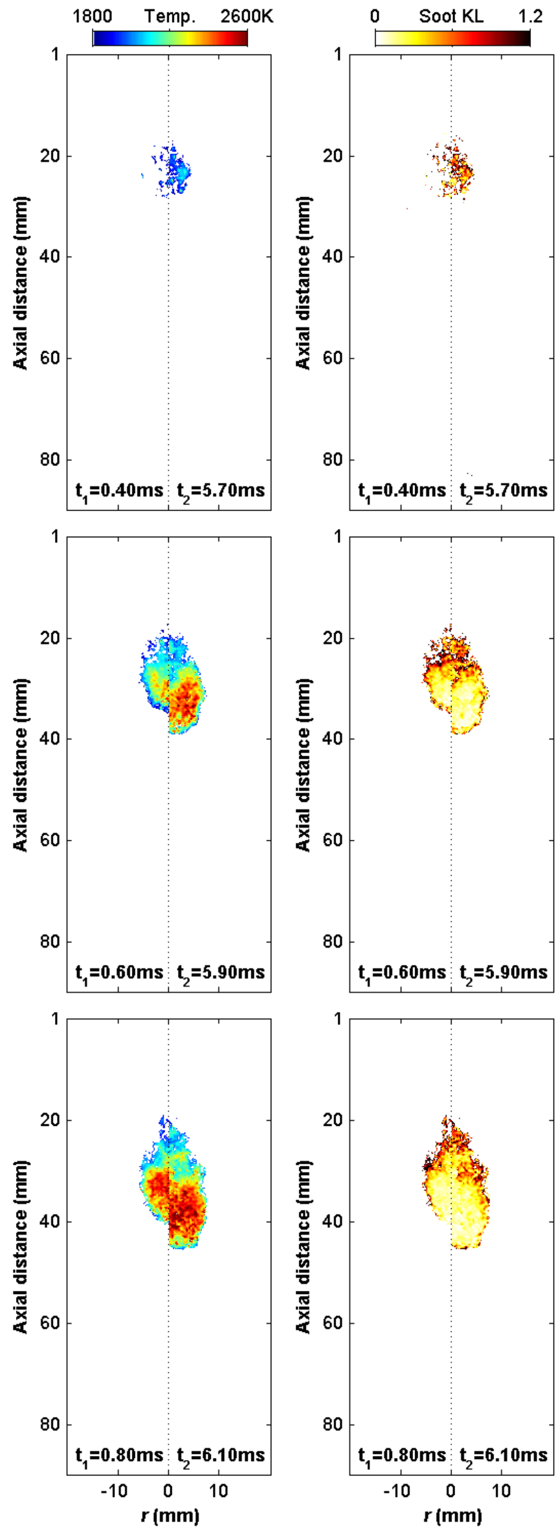

Figure 13: Comparisons of spatial distributions of typical, instantaneous soot temperature and soot KL of the main (left half) and post injections (right half), at three selected timing pairs, for the main-post case with a dwell time (DT) of 2.5 ms. The fuel is injected from the top to bottom, in these images. Ambient temperature: 900 K.

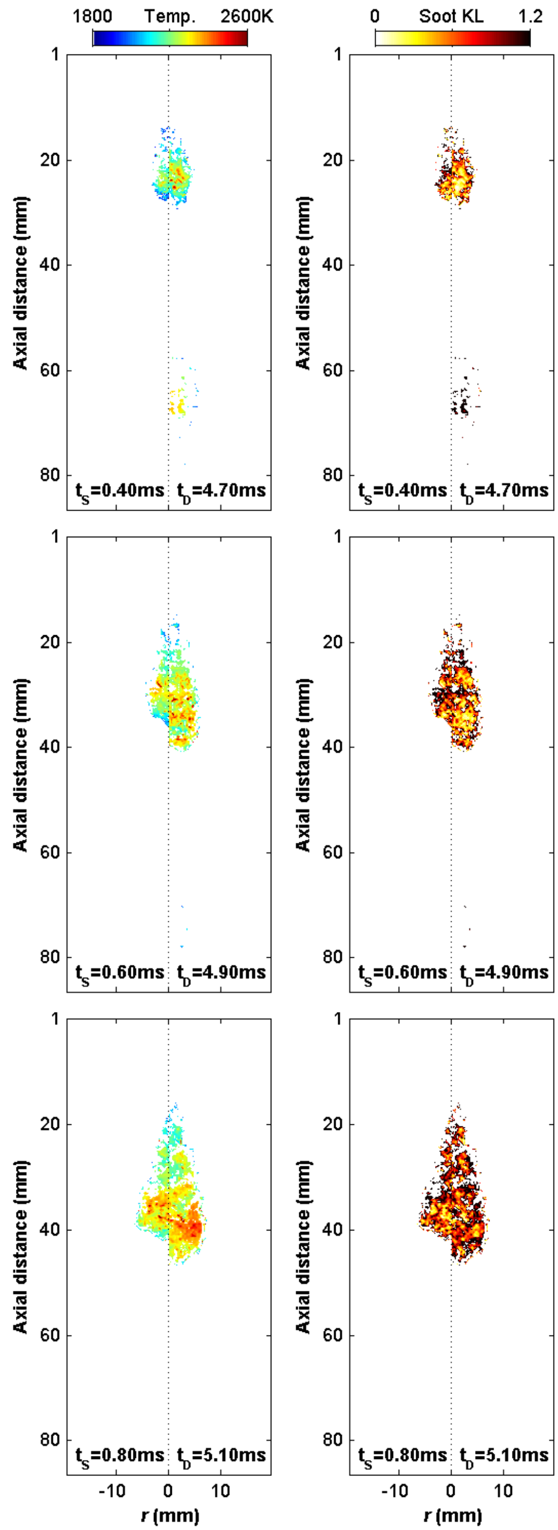

Figure 14: Comparisons of spatial distributions of typical, instantaneous soot temperature and soot KL of the main (left half) and post injections (right half), at three selected timing pairs, for the main-post case with a dwell time (DT) of 1.5 ms. The fuel is injected from the top to bottom, in these images. Ambient temperature: 1100 K.

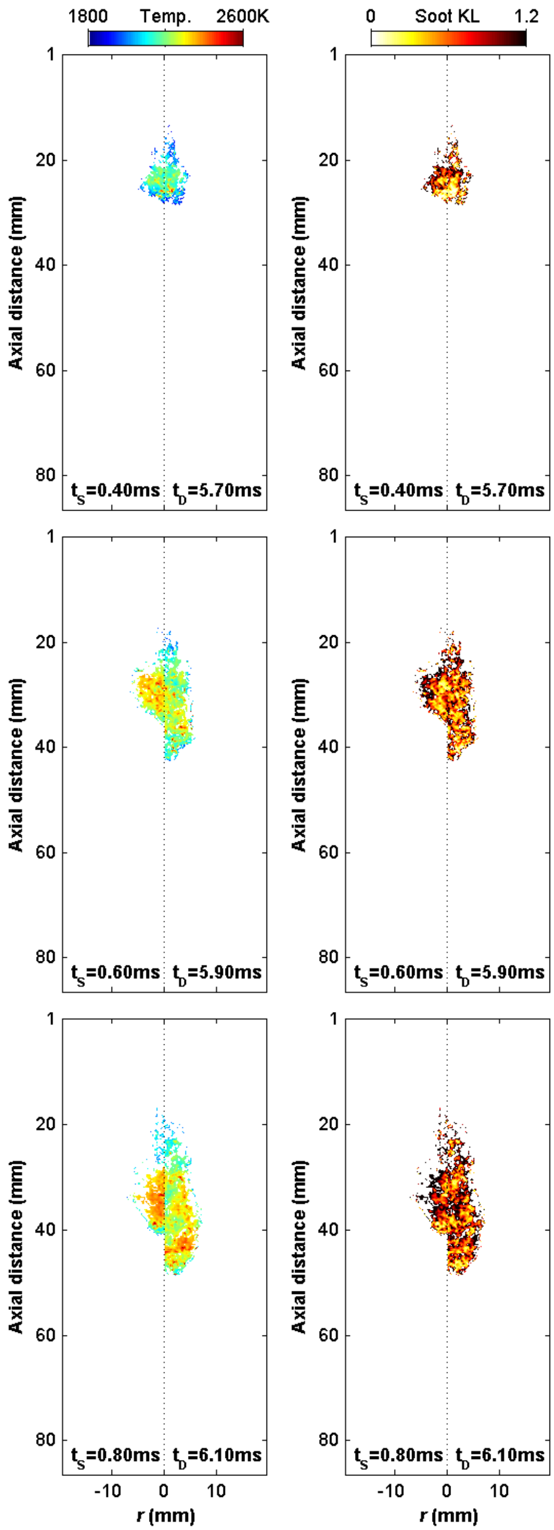

Figure 15: Comparisons of spatial distributions of typical, instantaneous soot temperature and soot KL of the main (left half) and post injections (right half), at three selected timing pairs, for the main-post case with a dwell time (DT) of 2.5 ms. The fuel is injected from the top to bottom, in these images. Ambient temperature: 1100 K.

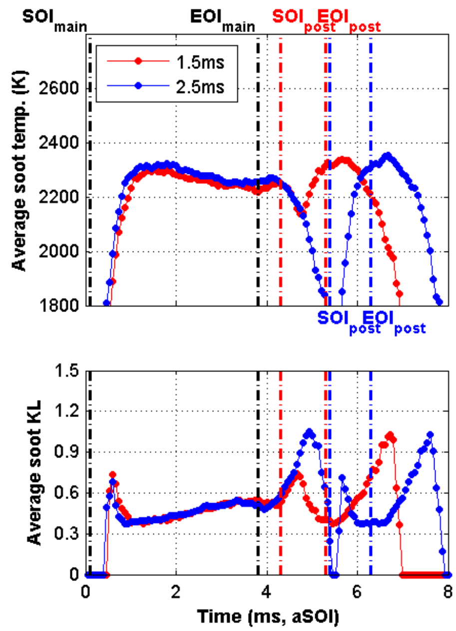

Figure 16: The time-resolved results for spatially-averaged soot two-color temperature (upper) and soot KL factor values (lower) for the main-post injection cases with dwell times (DTs) of 1.5 and 2.5 ms, respectively. The start of injection and end of injection timings for the main-post injection cases are indicated on the plots using dashed lines. Ambient temperature: 900 K.

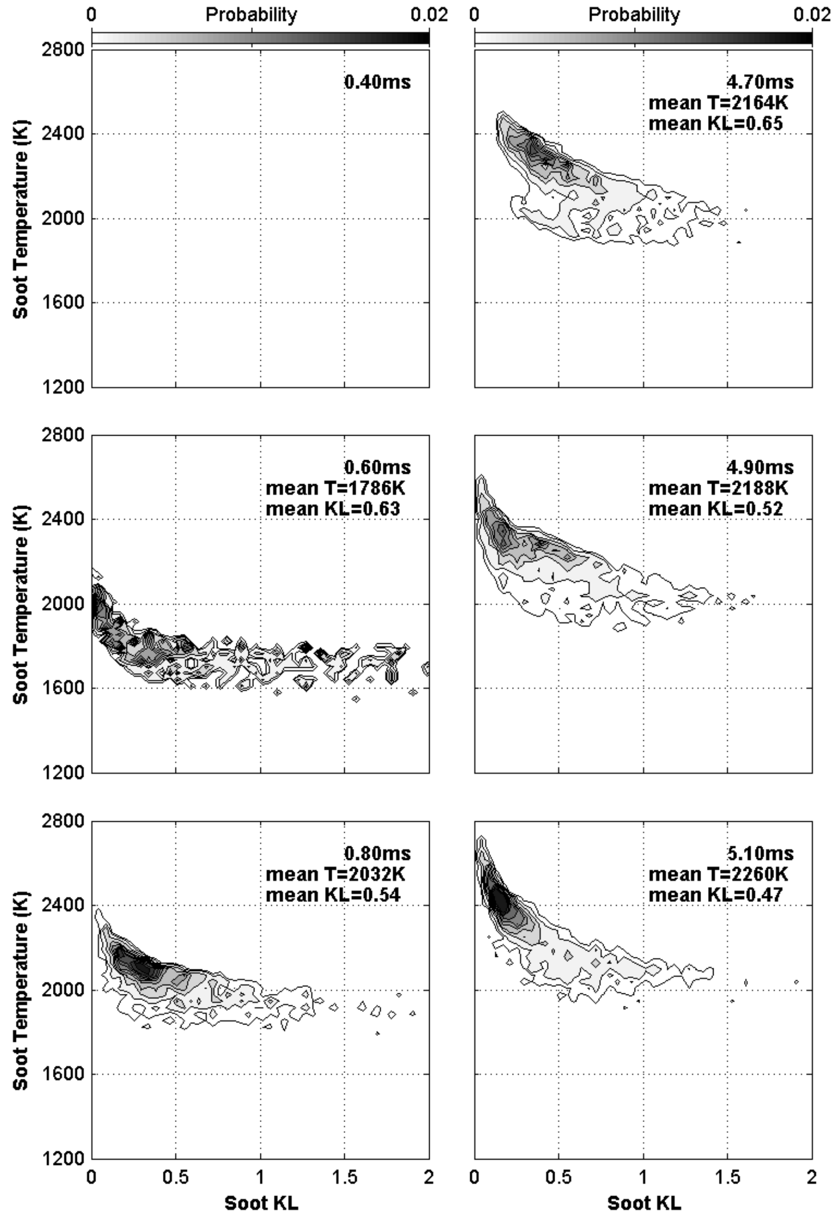

Figure 17: Comparisons of joint PDFs of soot temperature and soot KL of the main (left) and post (right) injections at three selected time steps, for a main-post injection case with a dwell time (DT) of 1.5 ms. All time instants have the same color scale. Ambient temperature: 900 K.

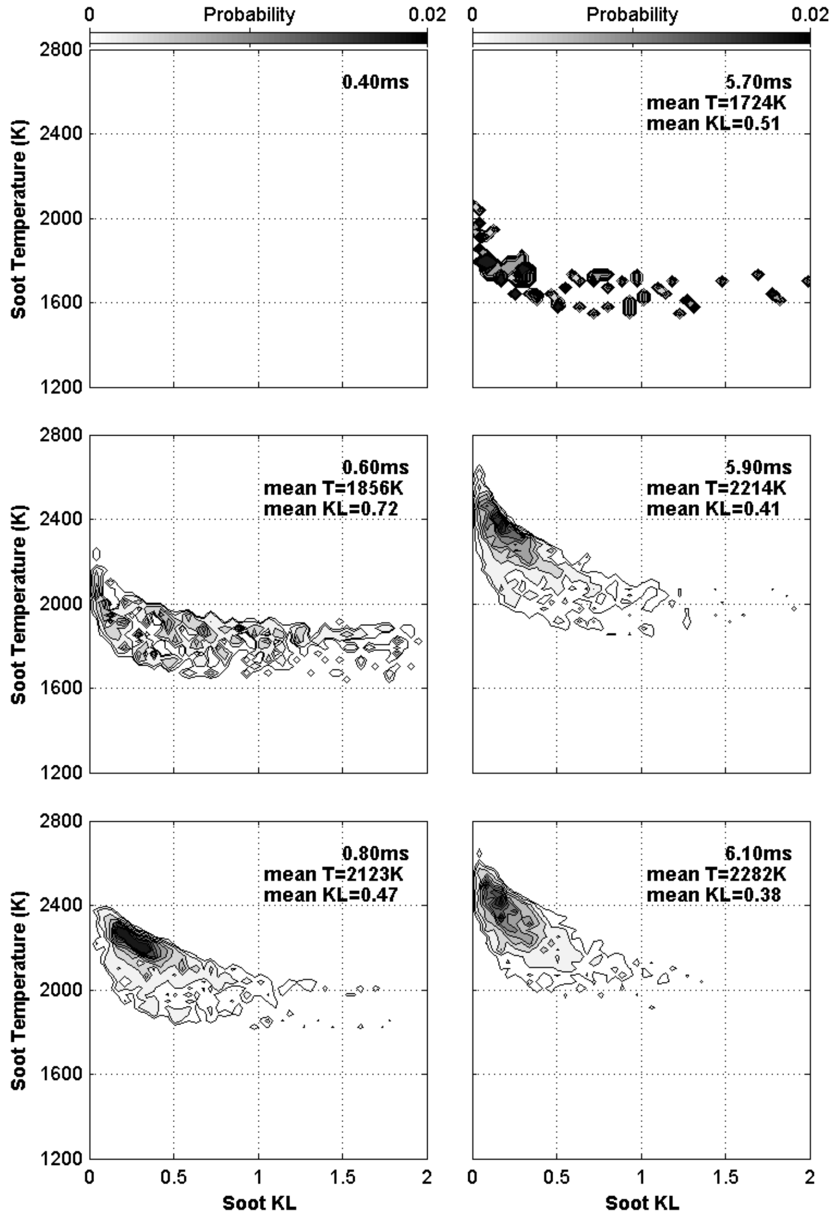

Figure 18: Comparisons of joint PDFs of soot temperature and soot KL of the main (left) and post (right) injections at three selected time steps, for a main-post injection case with a dwell time (DT) of 2.5 ms. All time instants have the same color scale. Ambient temperature: 900 K.

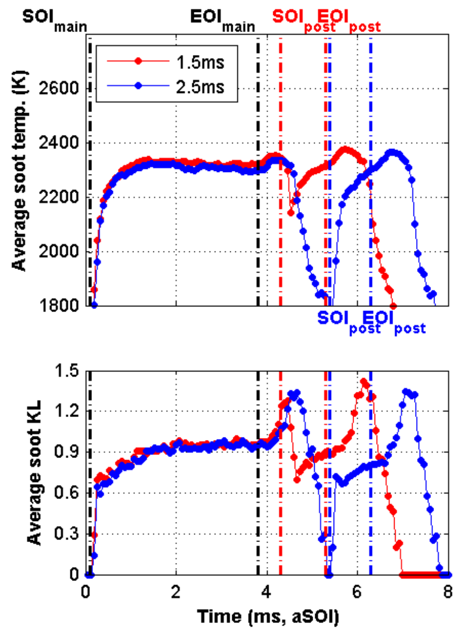

Figure 19: The time-resolved results for spatially-averaged soot two-color temperature (upper) and soot KL factor values (lower) for the main-post injection cases with dwell times (DTs) of 1.5 and 2.5 ms, respectively. The start of injection and end of injection timings for the main-post injection cases are indicated on the plots using dashed lines. Ambient temperature: 1100 K.

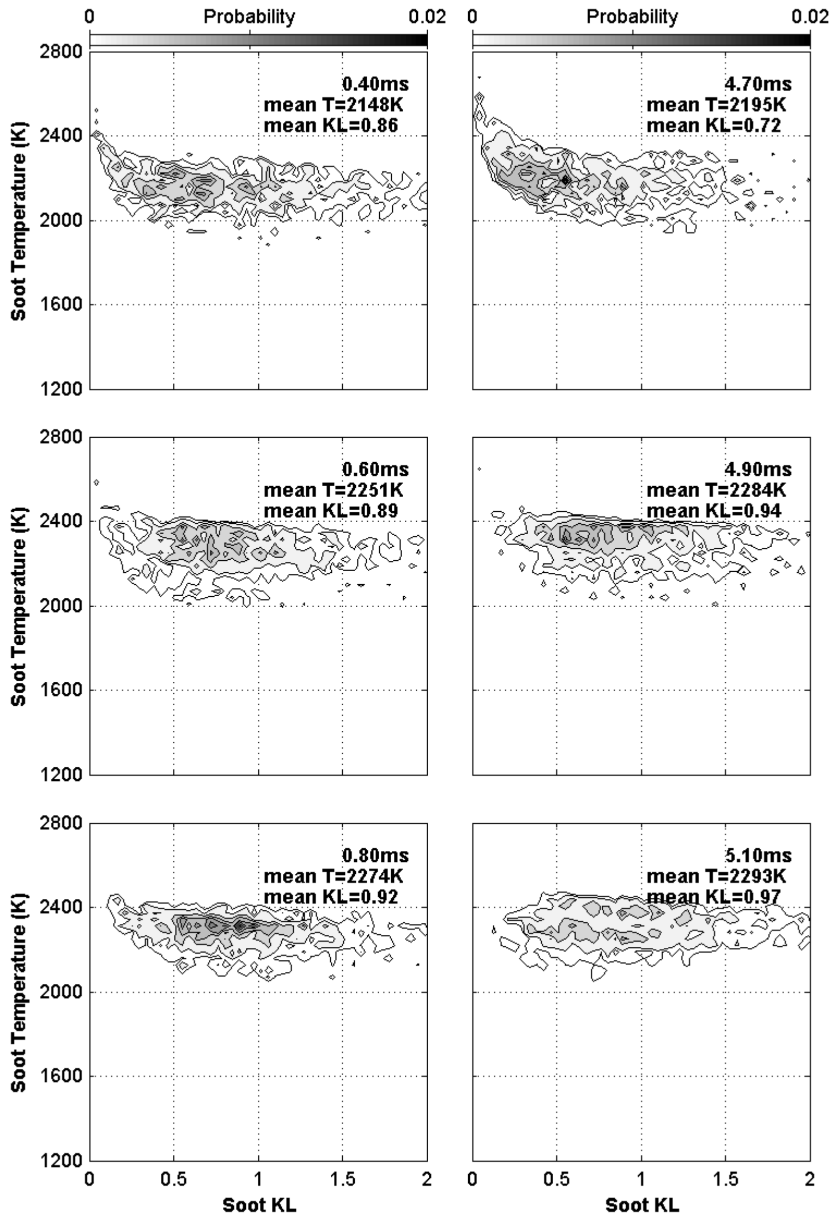

Figure 20: Comparisons of joint PDFs of soot temperature and soot KL of the main (left) and post (right) injections at three selected time steps, for a main-post injection case with a dwell time (DT) of 1.5 ms. All time instants have the same color scale. Ambient temperature: 1100 K.

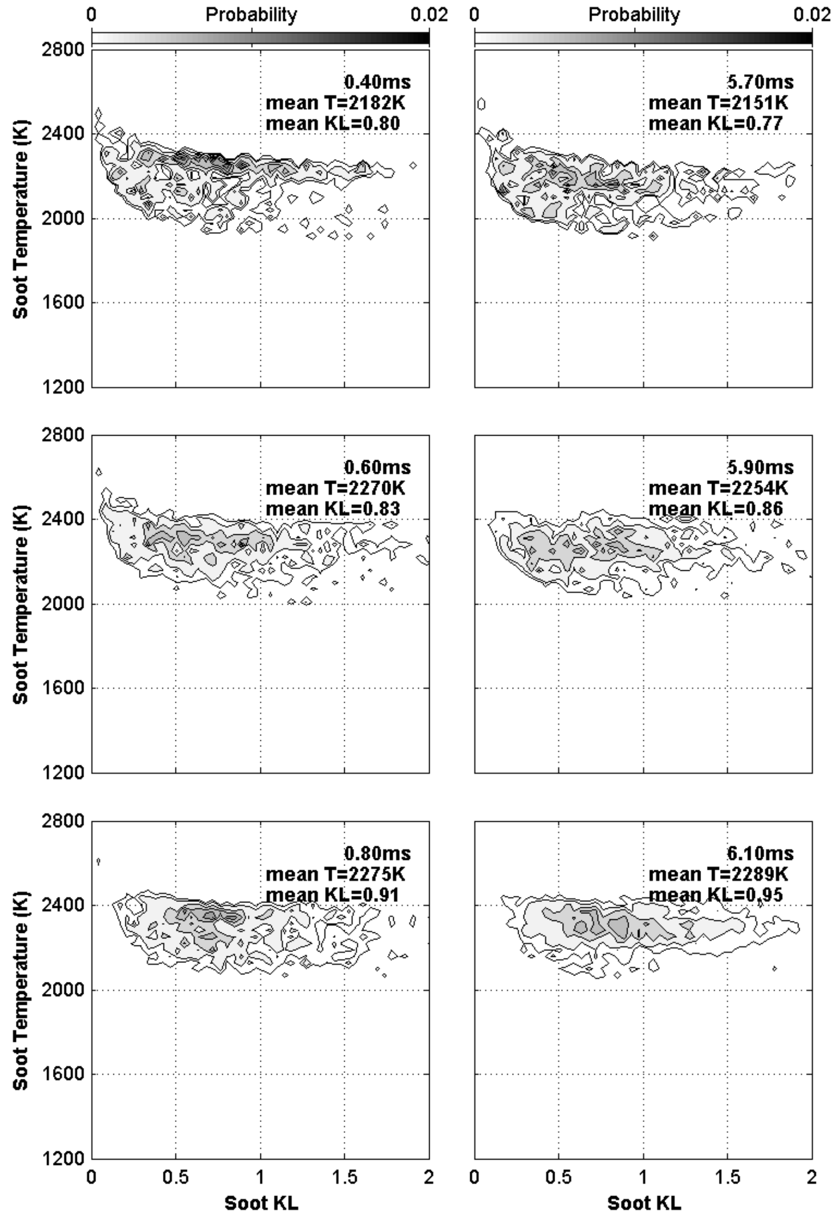

Figure 21: Comparisons of joint PDFs of soot temperature and soot KL of the main (left) and post (right) injections at three selected time steps, for a main-post injection case with a dwell time (DT) of 2.5 ms. All time instants have the same color scale. Ambient temperature: 1100 K.

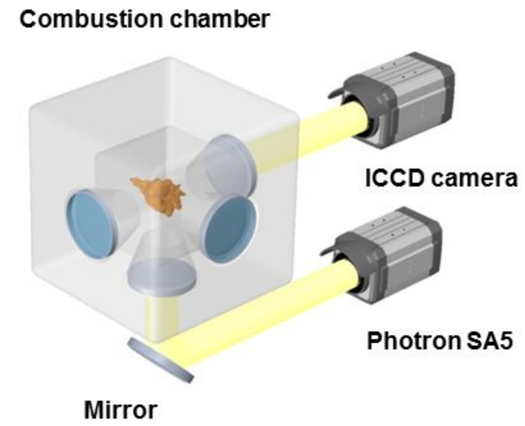
Combustion chamber
ICCD camera
Photron SA5
Mirror

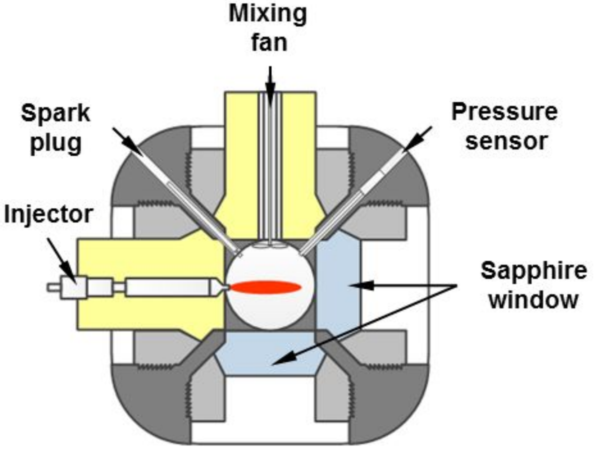
Mixing fan
Spark plug
Pressure sensor
Injector
Sapphire window

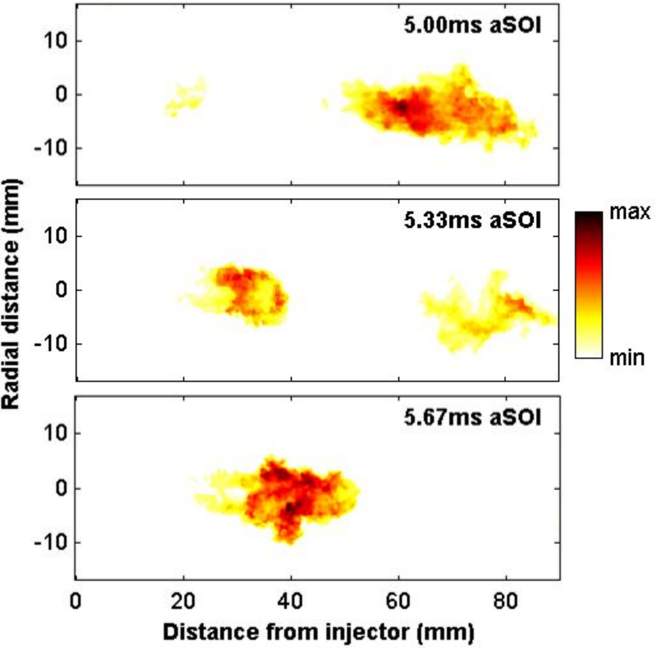

5.00ms aSOI
5.33ms aSOI
5.67ms aSOI
max
min
Radial distance (mm)
Distance from injector (mm)
10
0
-10
0
20
40
60
80

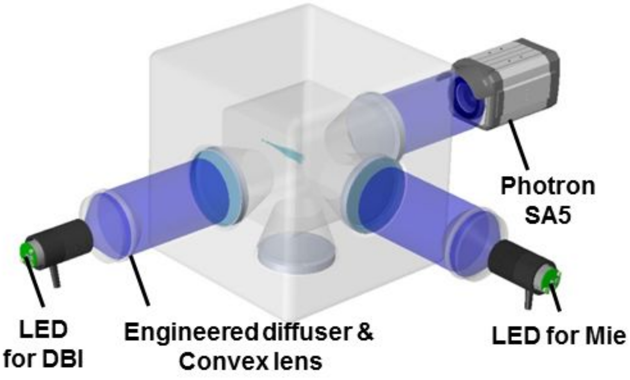
Photron
SA5
LED
for DBI
Engineered diffuser &
Convex lens
LED for Mie

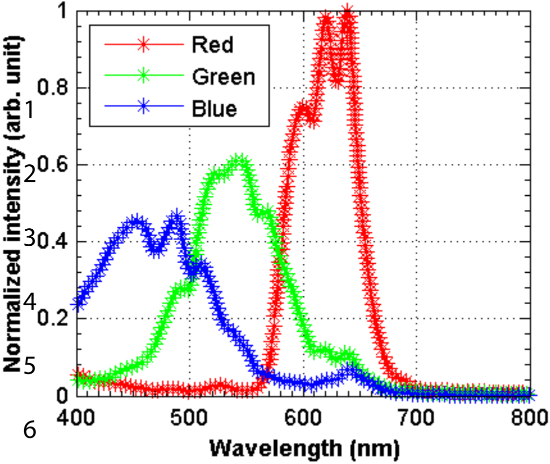
Red
Green
Blue
Normalized intensity (arb. unit)
Wavelength (nm)
0
0.2
0.4
0.6
0.8
1
400
500
600
700
800

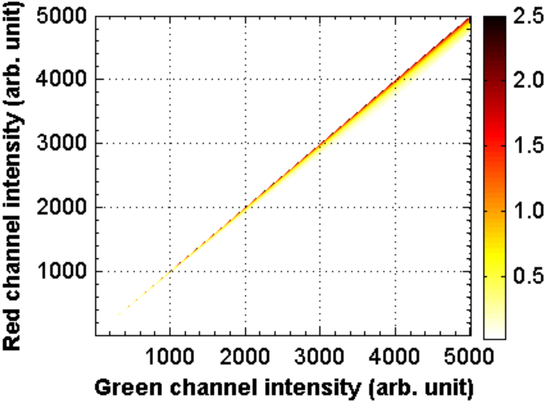
Red channel intensity (arb. unit)
Green channel intensity (arb. unit)
5000
4000
3000
2000
1000
1000
2000
3000
4000
5000
2.5
2.0
1.5
1.0
0.5

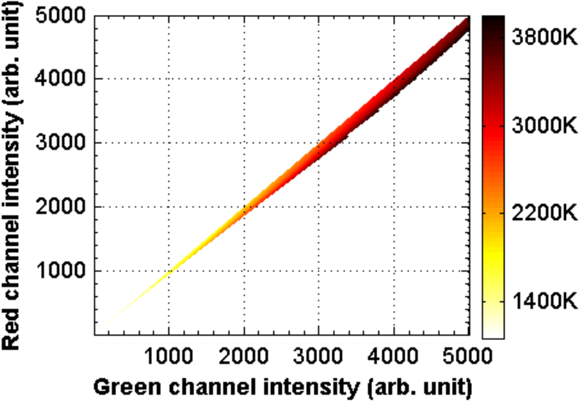

5000
4000
3000
2000
1000
1000
2000
3000
4000
5000
Red channel intensity (arb. unit)
Green channel intensity (arb. unit)
3800K
3000K
2200K
1400K

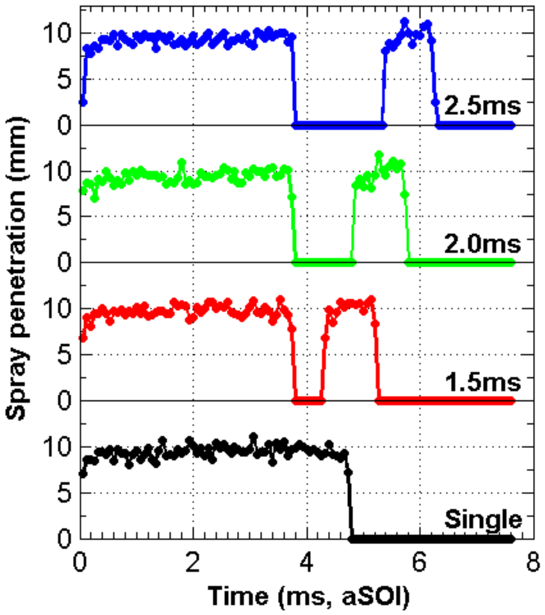
10
5
0
2.5ms
2.0ms
1.5ms
Single
Spray penetration (mm)
0
2
4
6
8
Time (ms, aSOI)

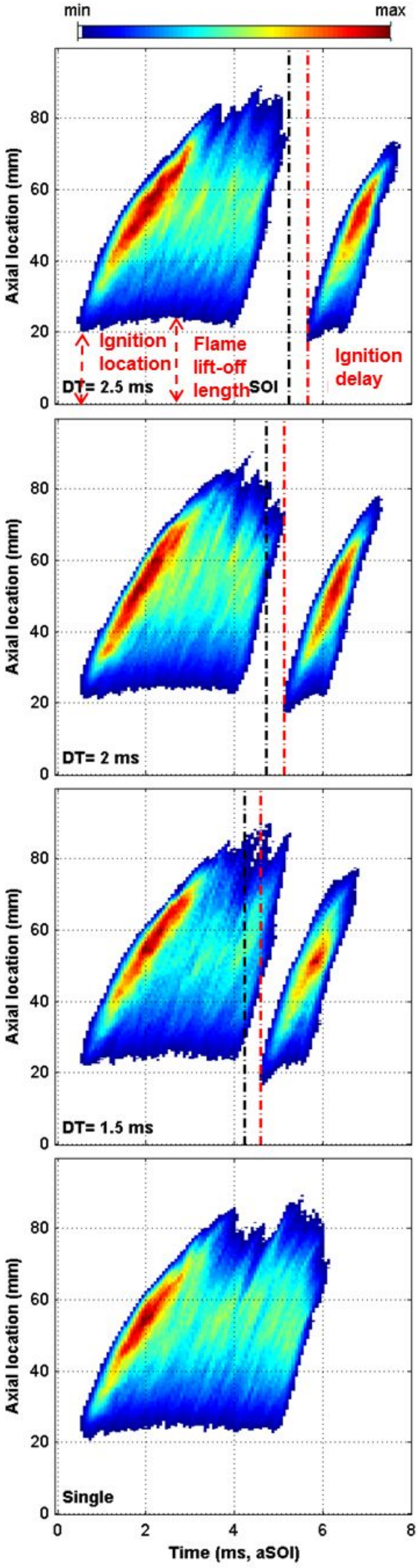

min
max
Axial location (mm)
Ignition location
Flame lift-off length
SOI
Ignition delay
DT= 2.5 ms
DT= 2 ms
DT= 1.5 ms
Single
Time (ms, aSOI)

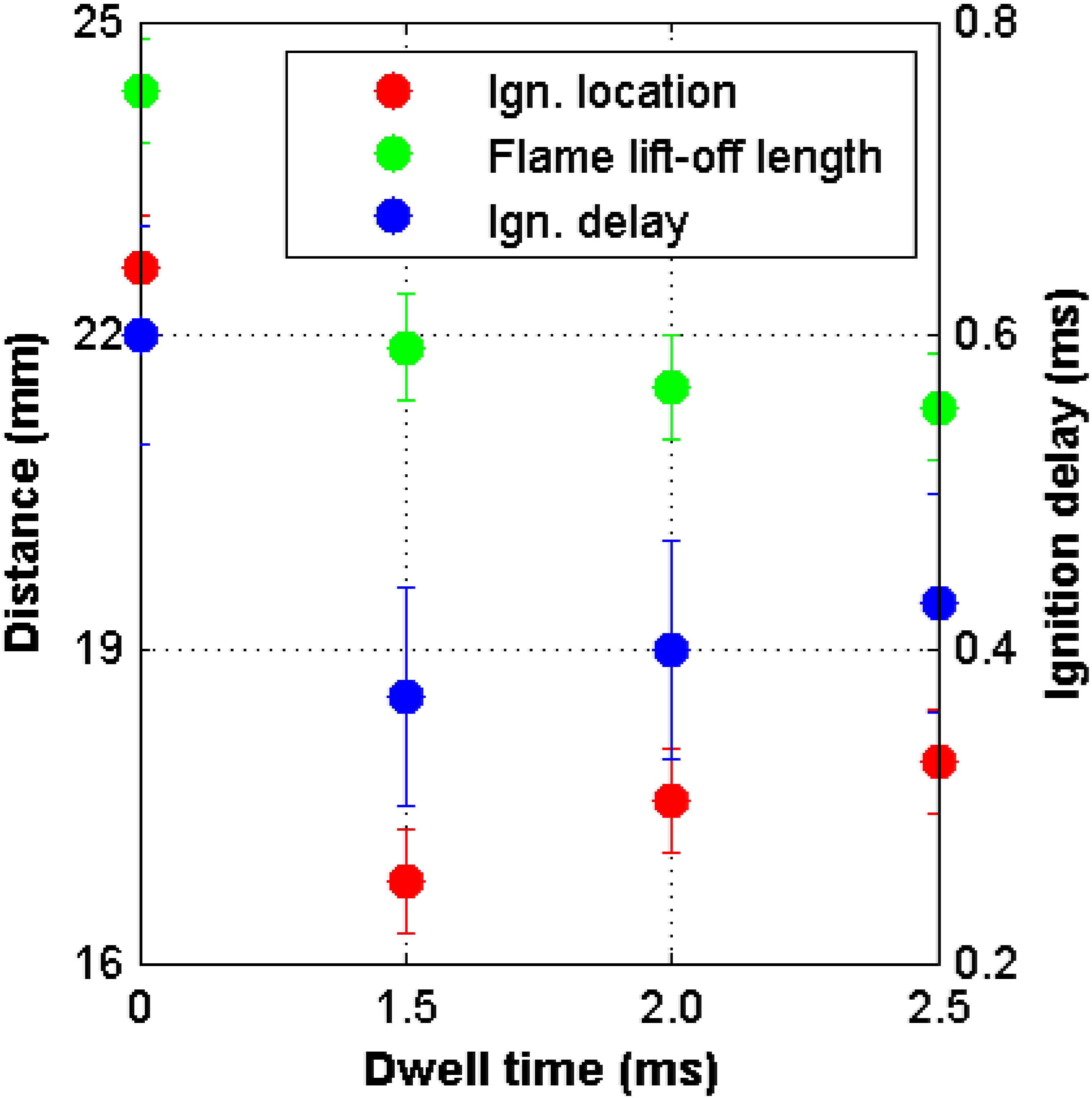

Ign. location
Flame lift-off length
Ign. delay
Distance (mm)
Ignition delay (ms)
Dwell time (ms)
25
22
19
16
0.8
0.6
0.4
0.2
0
1.5
2.0
2.5

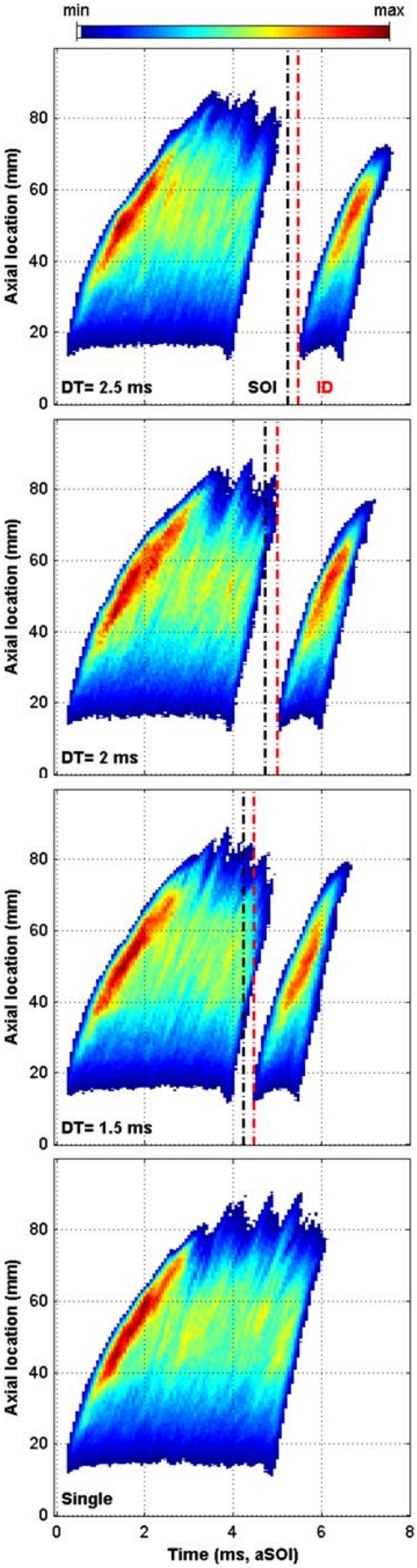

min
max
Axial location (mm)
DT= 2.5 ms
SOI
ID
DT= 2 ms
DT= 1.5 ms
Single
Time (ms, aSOI)

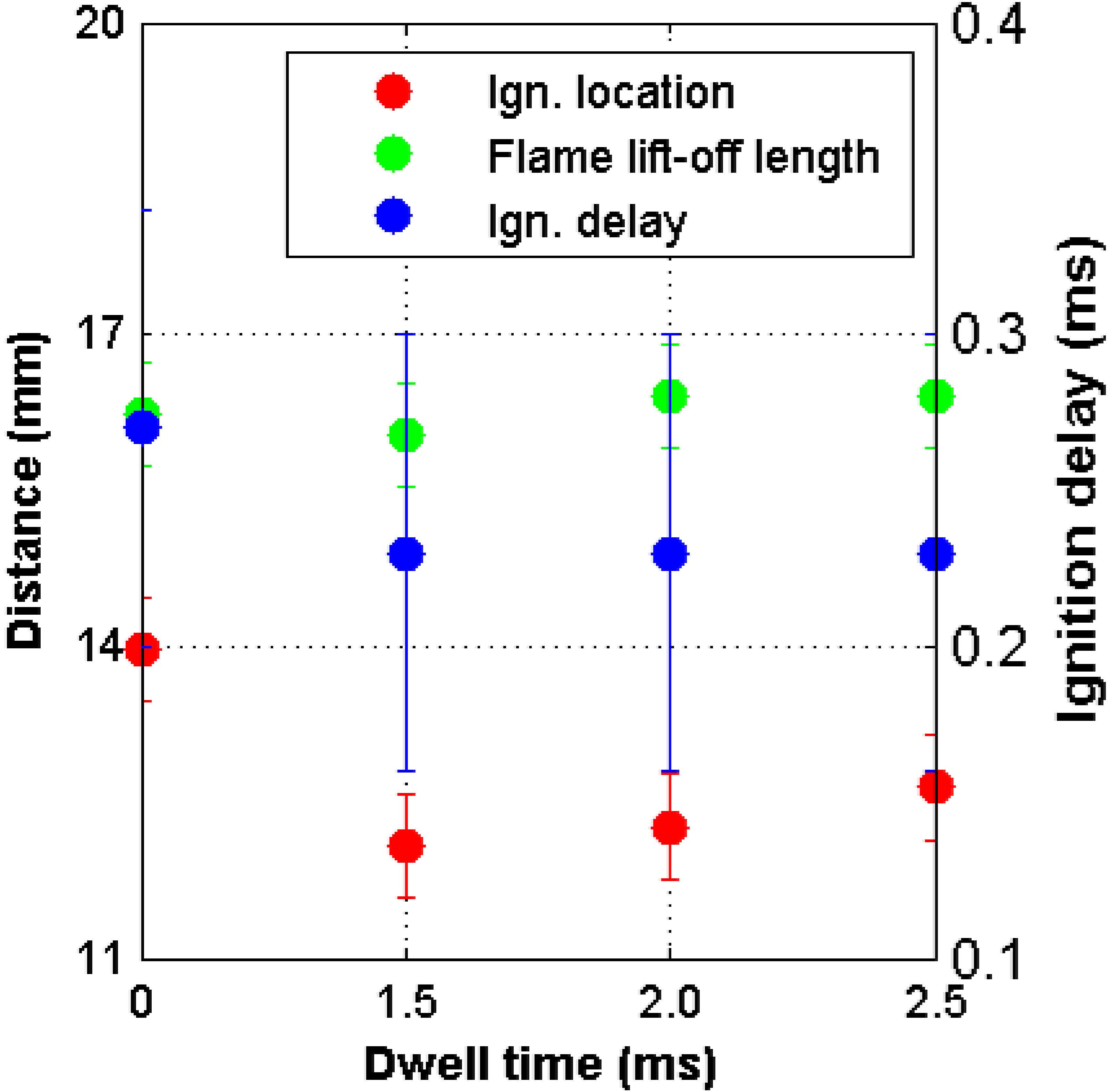

20
17
14
11
0.4
0.3
0.2
0.1
Ign. location
Flame lift-off length
Ign. delay
Distance (mm)
Ignition delay (ms)
0
1.5
2.0
2.5
Dwell time (ms)

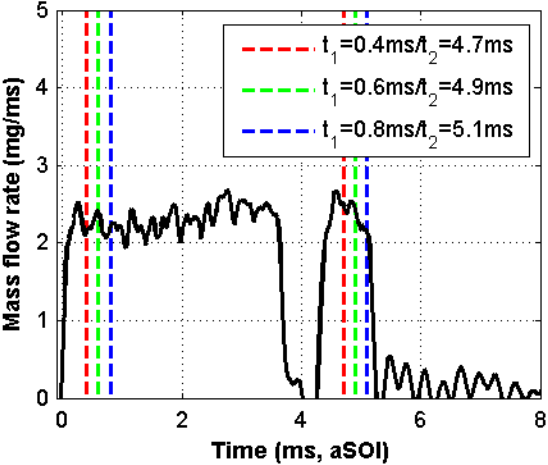

t1=0.4ms/t2=4.7ms
t1=0.6ms/t2=4.9ms
t1=0.8ms/t2=5.1ms
Mass flow rate (mg/ms)
Time (ms, aSOI)
0
1
2
3
4
5
0
2
4
6
8

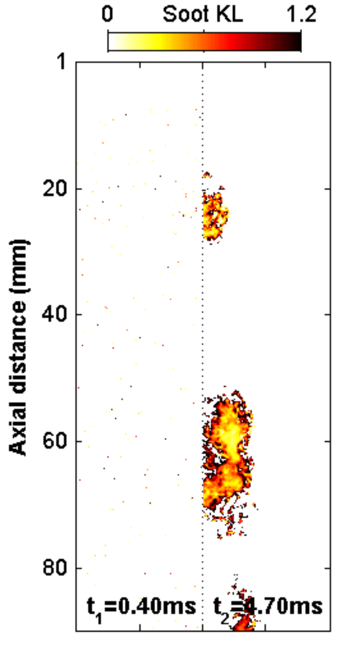

0
Soot KL
1.2
Axial distance (mm)
1
20
40
60
80
t1=0.40ms
t2=4.70ms

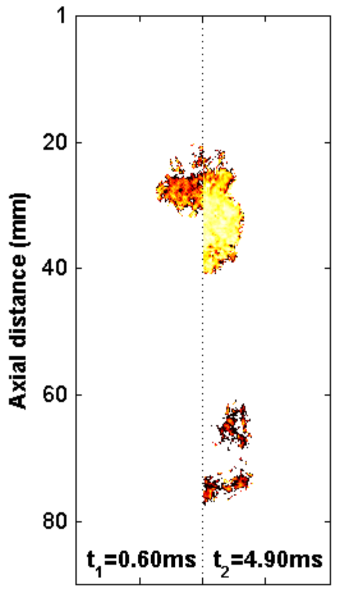

Axial distance (mm)
1
20
40
60
80
t1=0.60ms
t2=4.90ms

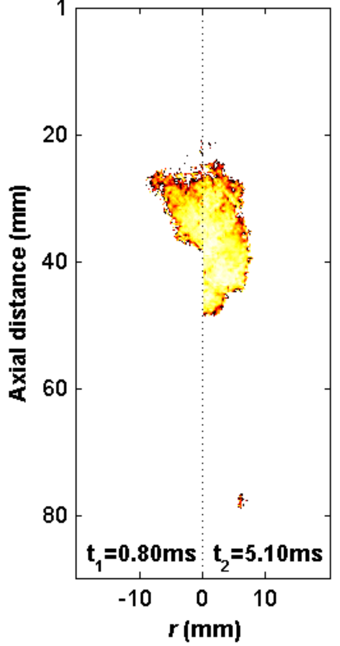

1
20
40
60
80
Axial distance (mm)
t1=0.80ms
t2=5.10ms
-10
0
10
r (mm)

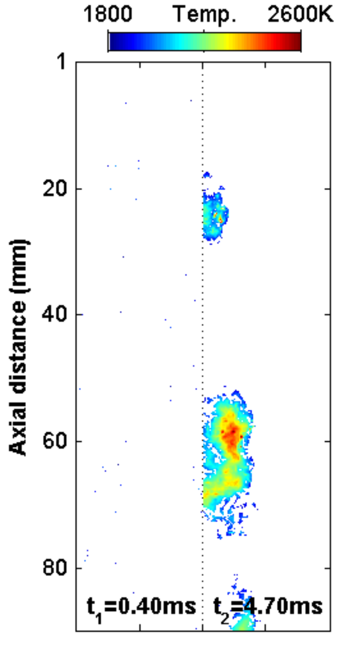

1800
Temp.
2600K
1
20
40
60
80
Axial distance (mm)
t_1=0.40ms
t_2=4.70ms

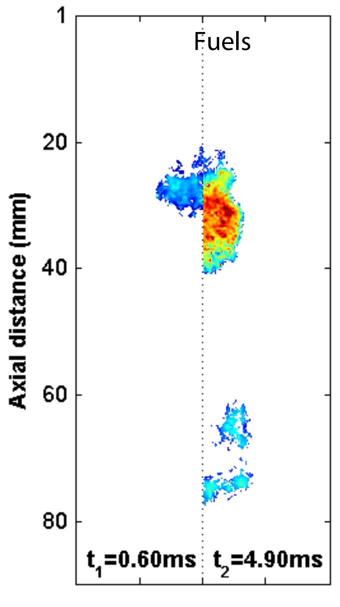

Fuels
Axial distance (mm)
1
20
40
60
80
t_1=0.60ms
t_2=4.90ms

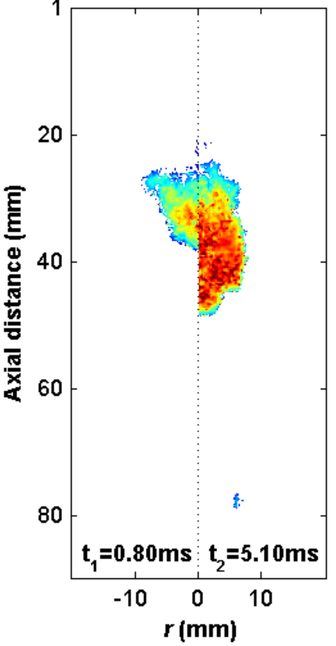

1
20
40
60
80
Axial distance (mm)
t1=0.80ms
t2=5.10ms
-10
0
10
r (mm)

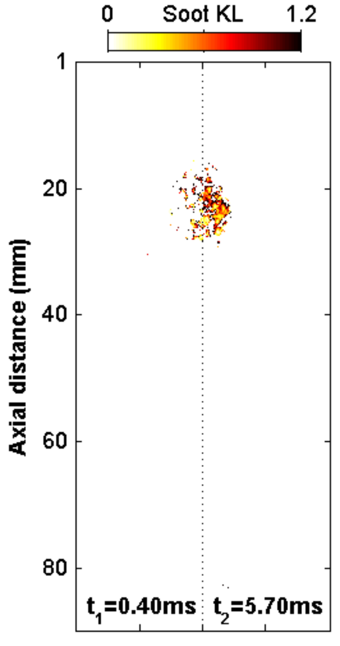

0
Soot KL
1.2
1
20
40
60
80
Axial distance (mm)
t_1=0.40ms
t_2=5.70ms

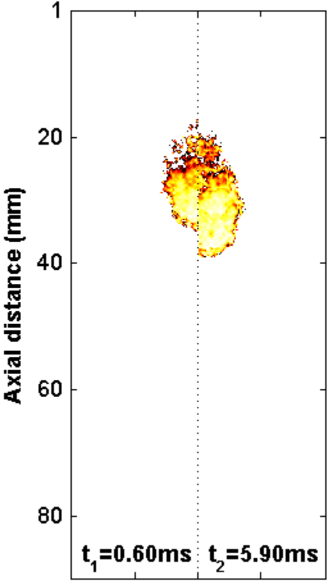

Axial distance (mm)
1
20
40
60
80
t1=0.60ms
t2=5.90ms

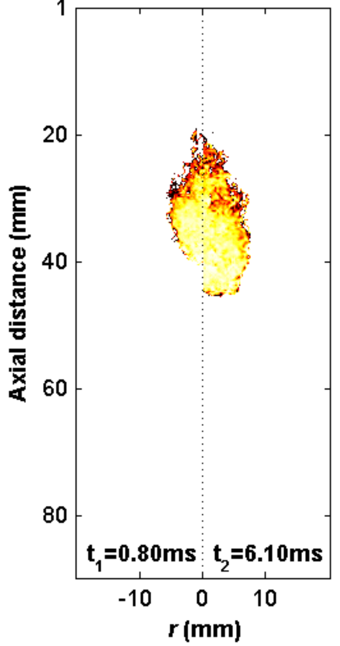

1
20
40
60
80
Axial distance (mm)
t1=0.80ms
t2=6.10ms
-10
0
10
r (mm)

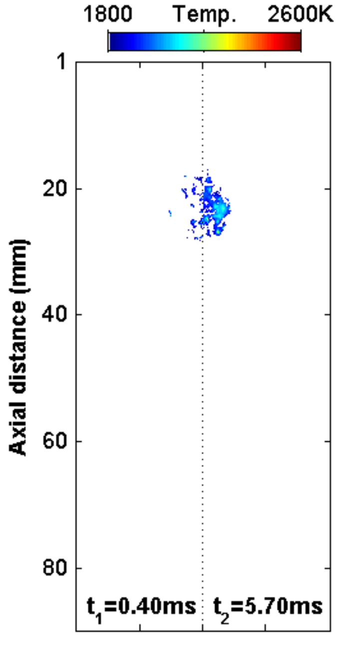
1800
Temp.
2600K
1
20
40
60
80
Axial distance (mm)
t_1=0.40ms
t_2=5.70ms

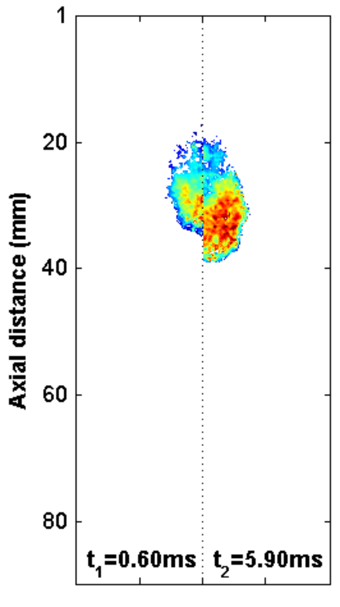

1
20
40
60
80
Axial distance (mm)
t_1=0.60ms
t_2=5.90ms

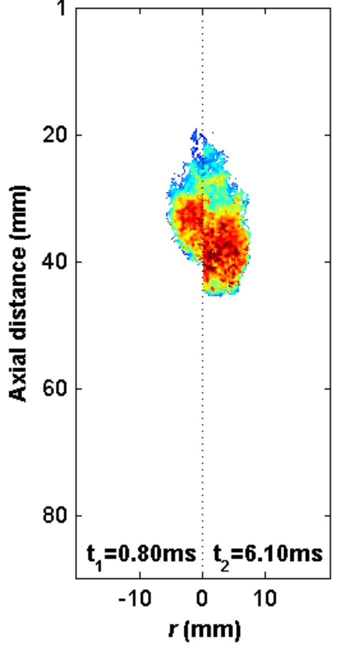

1
20
40
60
80
Axial distance (mm)
t1=0.80ms
t2=6.10ms
-10
0
10
r (mm)

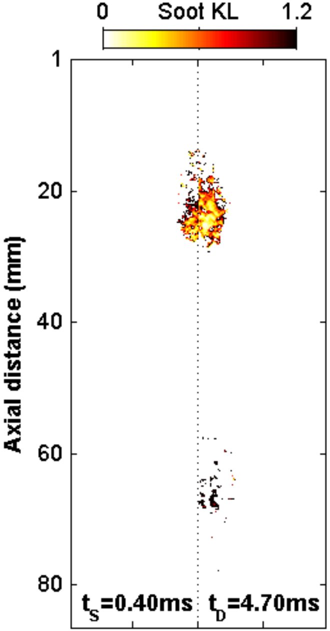

0
Soot KL
1.2
1
20
40
60
80
Axial distance (mm)
t_S=0.40ms
t_D=4.70ms

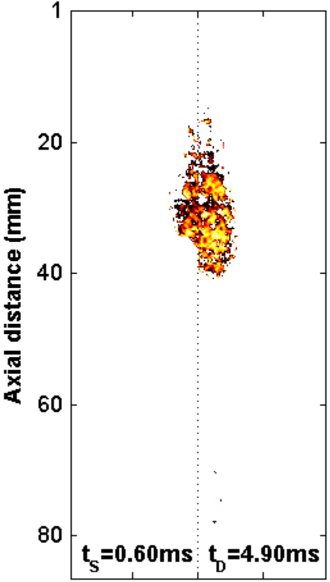

1
20
40
60
80
Axial distance (mm)
t_S=0.60ms
t_D=4.90ms

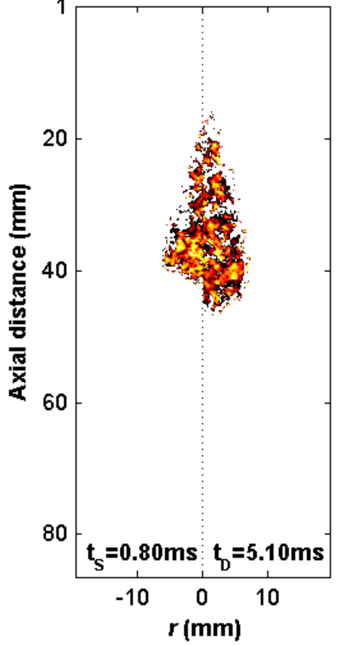

1
20
40
60
80
Axial distance (mm)
-10
0
10
r (mm)
t_S=0.80ms
t_D=5.10ms

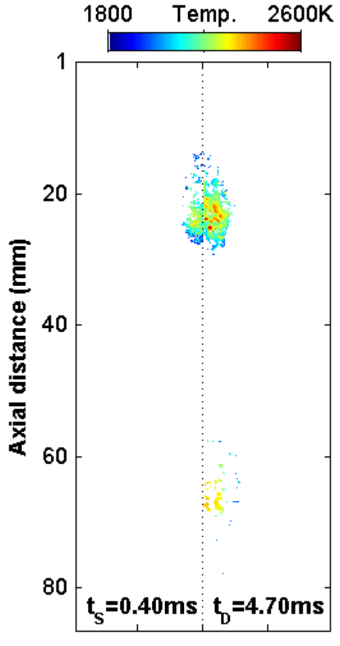

1800
Temp.
2600K
1
20
40
60
80
Axial distance (mm)
t_S=0.40ms
t_D=4.70ms

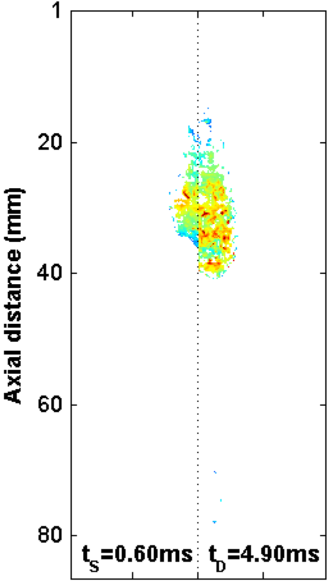

1
20
40
60
80
Axial distance (mm)
t_S=0.60ms
t_D=4.90ms

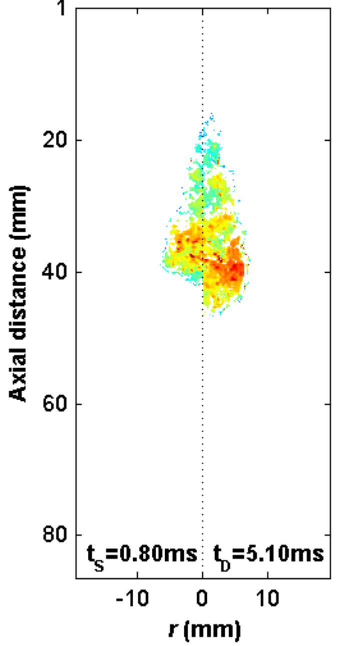

Axial distance (mm)
1
20
40
60
80
-10
0
10
r (mm)
tS=0.80ms
tD=5.10ms

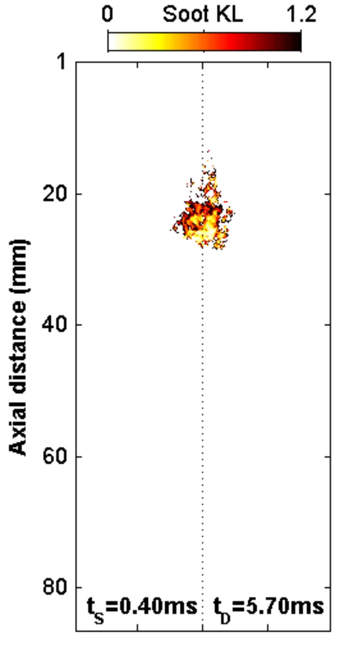

0
Soot KL
1.2
1
20
40
60
80
Axial distance (mm)
t_S=0.40ms
t_D=5.70ms

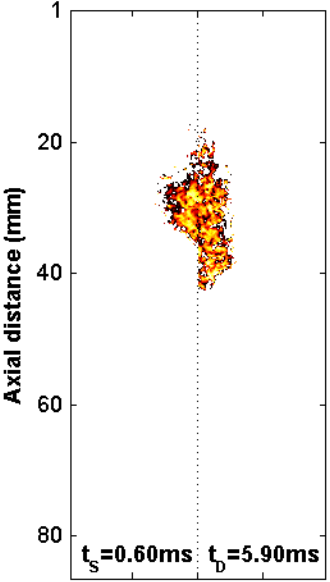
1
20
40
60
80
Axial distance (mm)
t_S=0.60ms
t_D=5.90ms

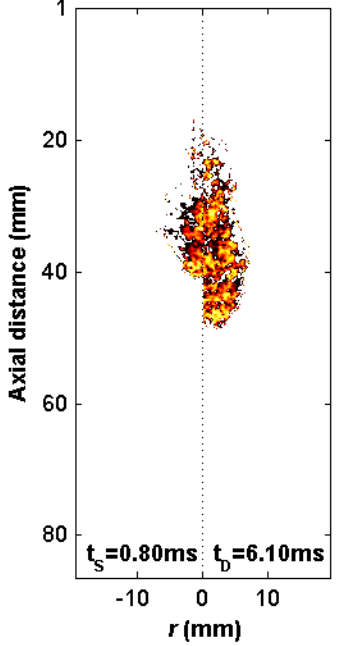

1
20
40
60
80
Axial distance (mm)
-10
0
10
r (mm)
t_S=0.80ms
t_D=6.10ms

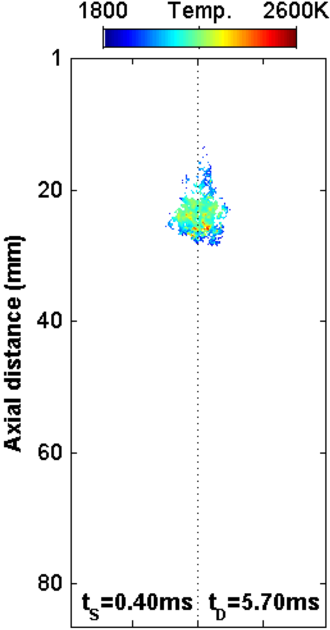

1800
Temp.
2600K
1
20
40
60
80
Axial distance (mm)
t_S=0.40ms
t_D=5.70ms

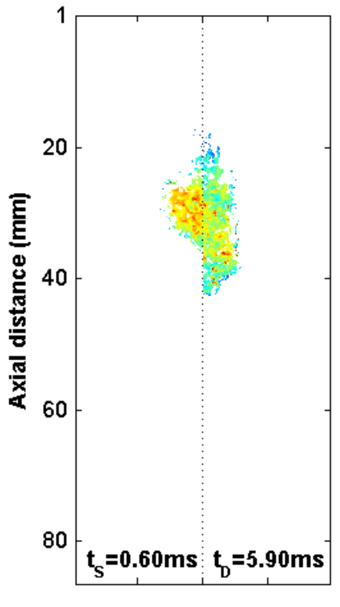

1
20
40
60
80
Axial distance (mm)
t_S=0.60ms
t_D=5.90ms

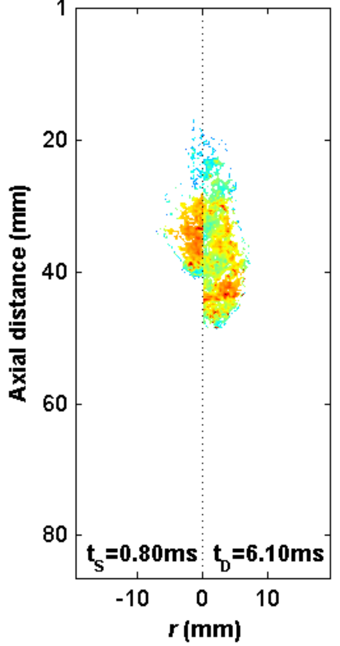

1
20
40
60
80
Axial distance (mm)
-10
0
10
r (mm)
t_S=0.80ms
t_D=6.10ms

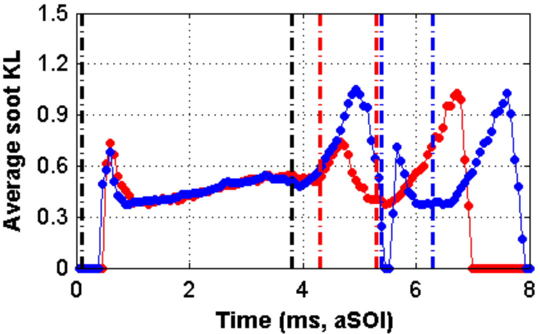
1.5
1.2
0.9
0.6
0.3
0
Average soot KL
0
2
4
6
8
Time (ms, aSOI)

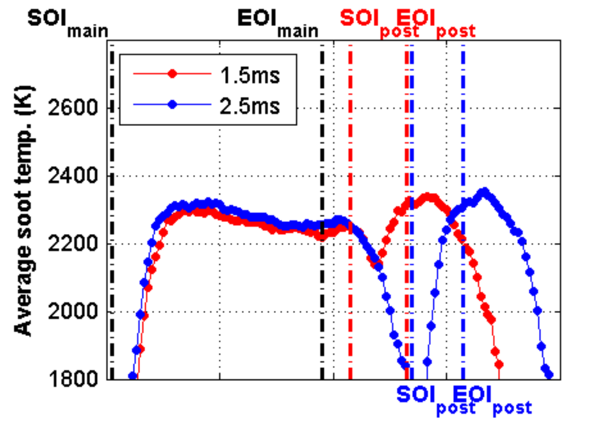

SOImain
EOImain
SOIpost
EOIpost
1.5ms
2.5ms
Average soot temp. (K)
2600
2400
2200
2000
1800
SOIpost
EOIpost

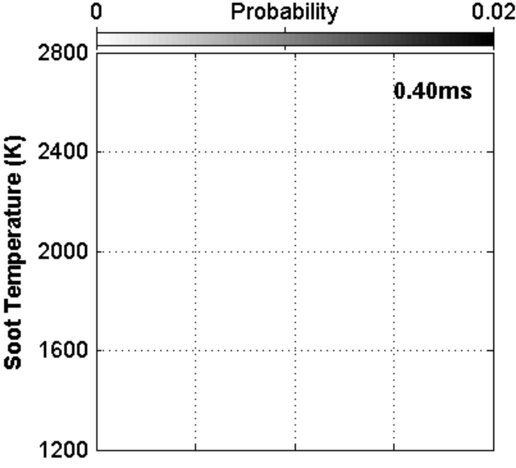

0
Probability
0.02
2800
2400
2000
1600
1200
0.40ms
Soot Temperature (K)

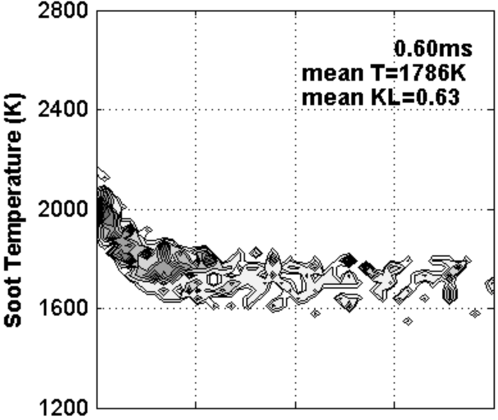
0.60ms
mean T=1786K
mean KL=0.63
Soot Temperature (K)
2800
2400
2000
1600
1200

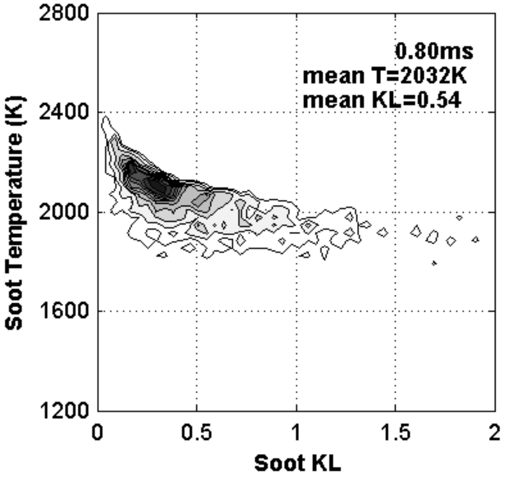

0.80ms
mean T=2032K
mean KL=0.54
Soot Temperature (K)
2800
2400
2000
1600
1200
0
0.5
1
1.5
2
Soot KL

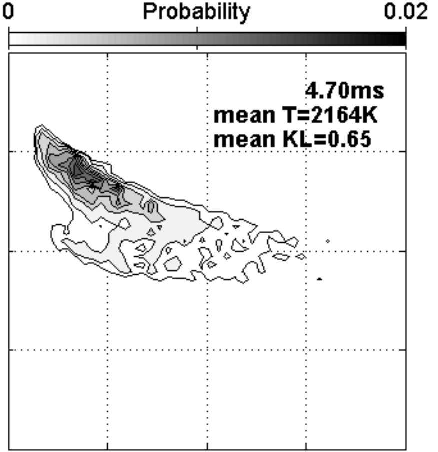

0
Probability
0.02
4.70ms
mean T=2164K
mean KL=0.65

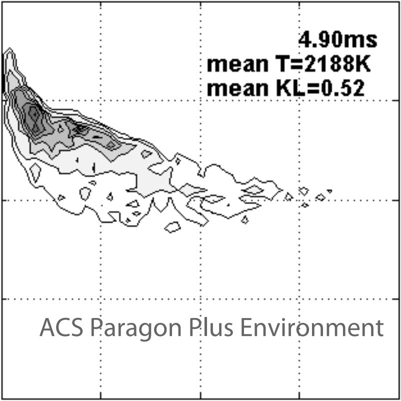
4.90ms
mean T=2188K
mean KL=0.52

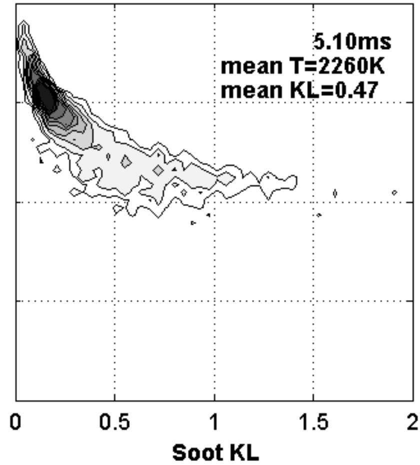
5.10ms
mean T=2260K
mean KL=0.47
0
0.5
1
1.5
2
Soot KL

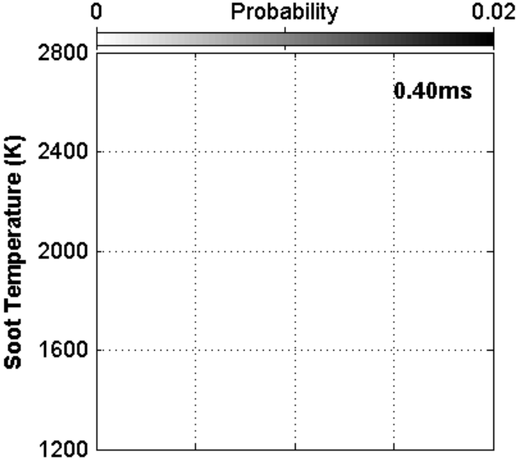
0
Probability
0.02
2800
0.40ms
2400
Soot Temperature (K)
2000
1600
1200

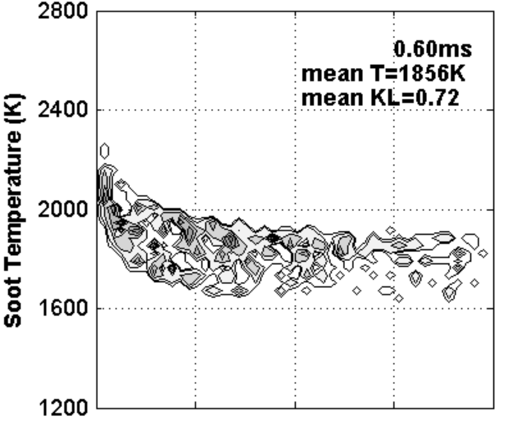

2800
2400
2000
1600
1200
Soot Temperature (K)
0.60ms
mean T=1856K
mean KL=0.72

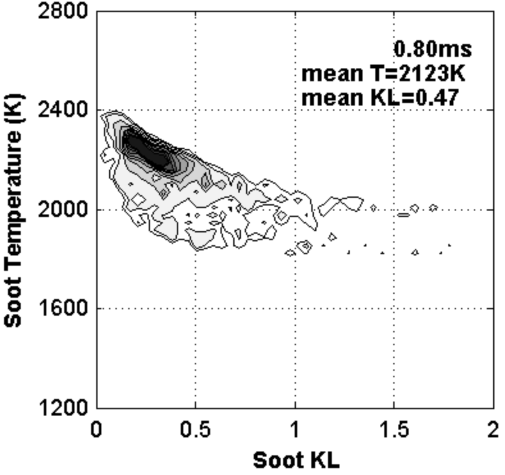

0.80ms
mean T=2123K
mean KL=0.47
Soot Temperature (K)
2800
2400
2000
1600
1200
0
0.5
1
1.5
2
Soot KL

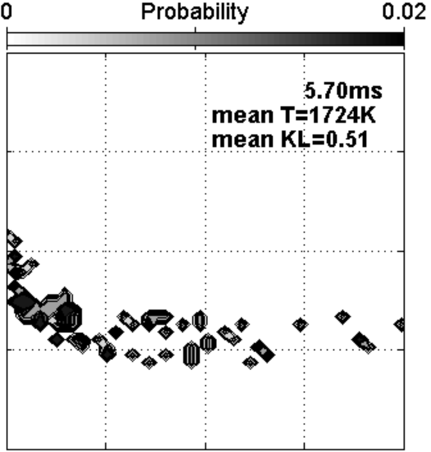
0
Probability
0.02
5.70ms
mean T=1724K
mean KL=0.51

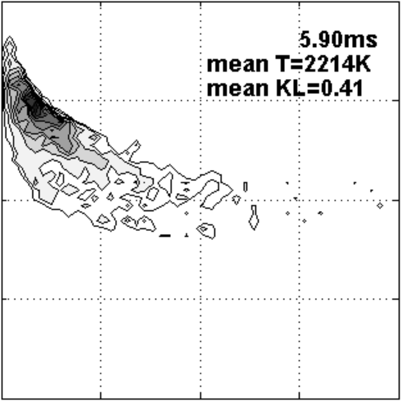
5.90ms
mean T=2214K
mean KL=0.41

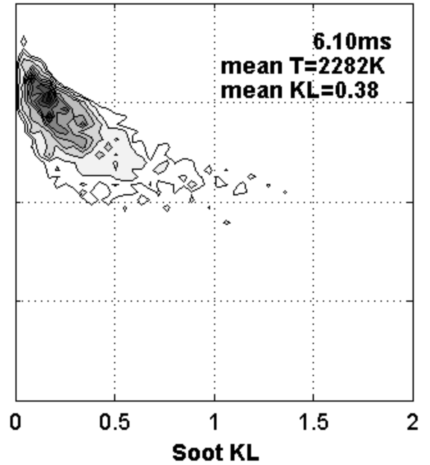
6.10ms
mean T=2282K
mean KL=0.38
0
0.5
1
1.5
2
Soot KL

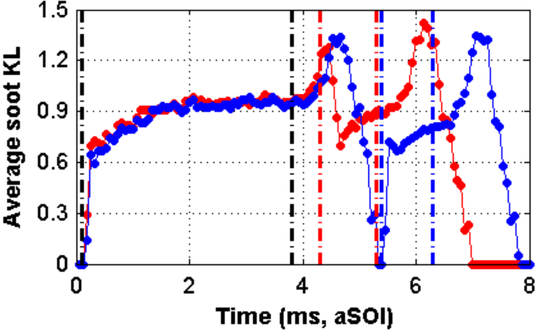

Average soot KL
Time (ms, aSOI)
0
0.3
0.6
0.9
1.2
1.5
0
2
4
6
8

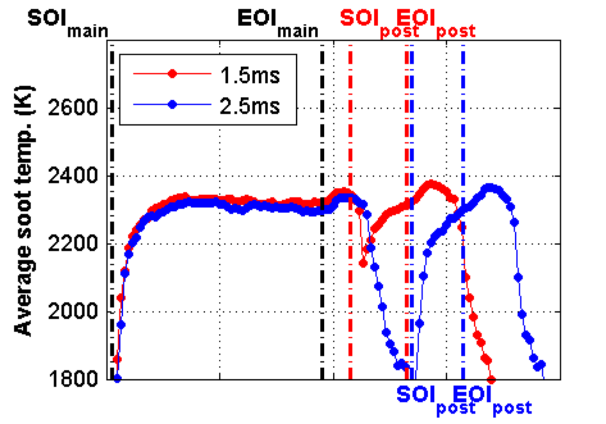

SOImain
EOImain
SOIpost
EOIpost
1.5ms
2.5ms
Average soot temp. (K)
2600
2400
2200
2000
1800
SOIpost
EOIpost

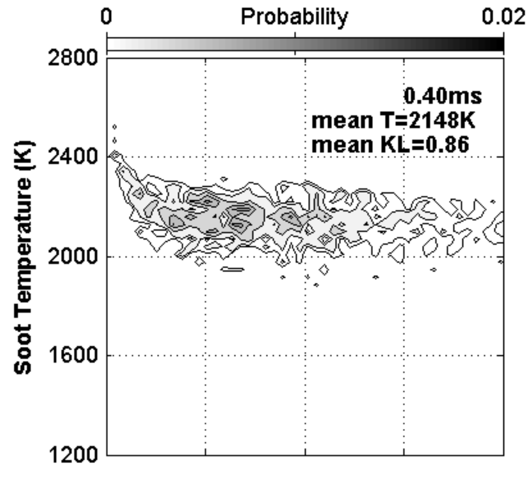

0
Probability
0.02
0.40ms
mean T=2148K
mean KL=0.86
2800
2400
2000
1600
1200
Soot Temperature (K)

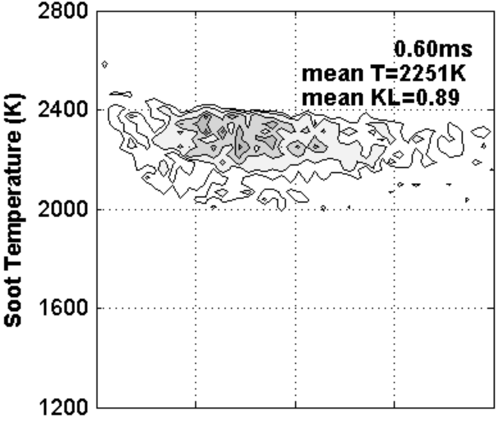
0.60ms
mean T=2251K
mean KL=0.89
Soot Temperature (K)
2800
2400
2000
1600
1200

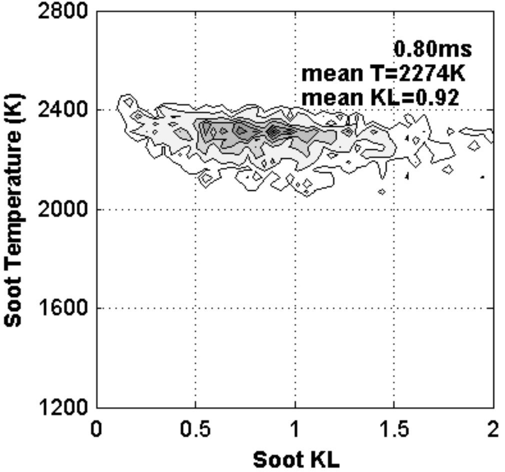

0.80ms
mean T=2274K
mean KL=0.92
Soot Temperature (K)
2800
2400
2000
1600
1200
0
0.5
1
1.5
2
Soot KL

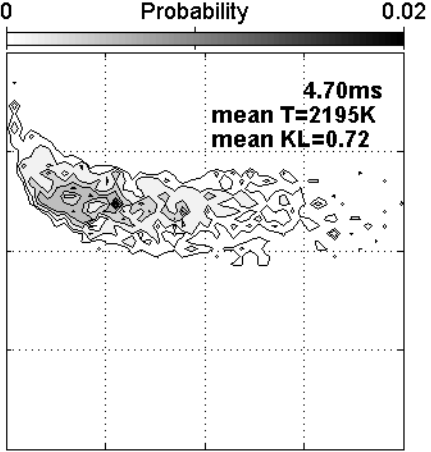
0
Probability
0.02
4.70ms
mean T=2195K
mean KL=0.72

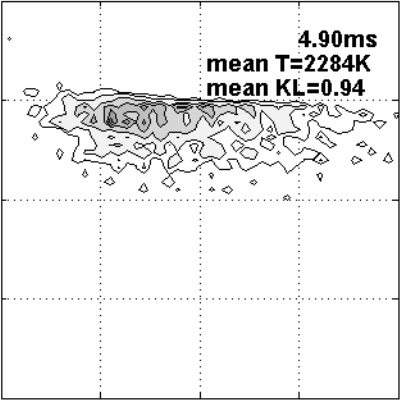

4.90ms
mean T=2284K
mean KL=0.94

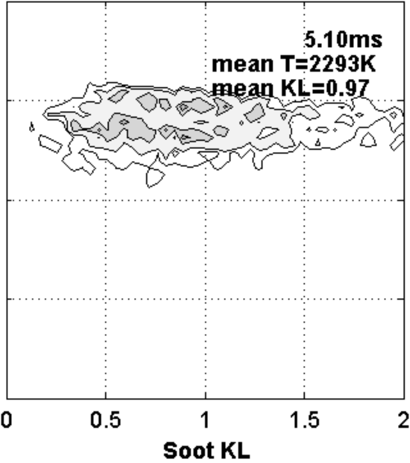

5.10ms
mean T=2293K
mean KL=0.97
0
0.5
1
1.5
2
Soot KL

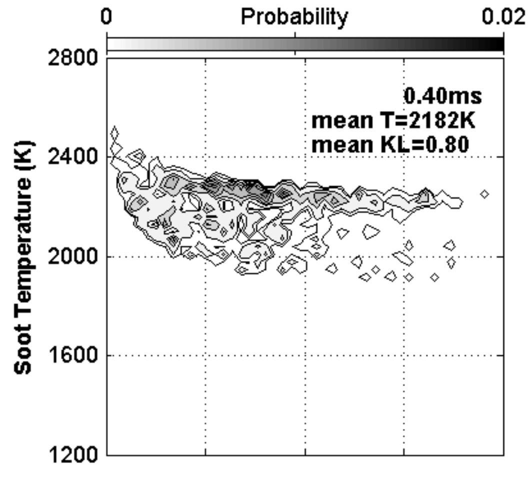

0
Probability
0.02
2800
2400
2000
1600
1200
Soot Temperature (K)
0.40ms
mean T=2182K
mean KL=0.80

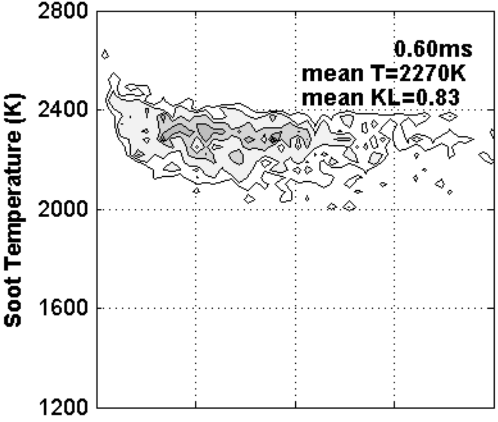

2800
2400
2000
1600
1200
Soot Temperature (K)
0.60ms
mean T=2270K
mean KL=0.83

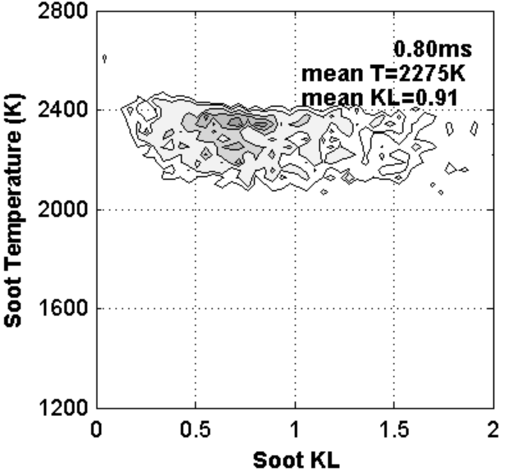

0.80ms
mean T=2275K
mean KL=0.91
Soot Temperature (K)
2800
2400
2000
1600
1200
0
0.5
1
1.5
2
Soot KL

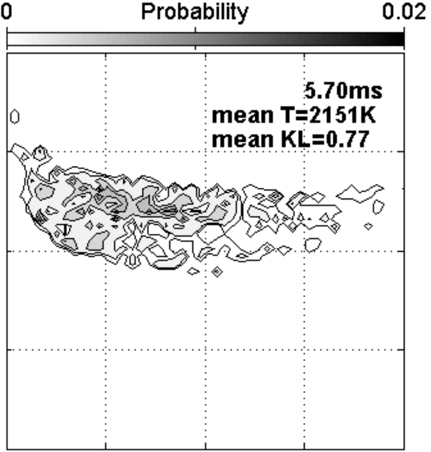
0
Probability
0.02
5.70ms
mean T=2151K
mean KL=0.77

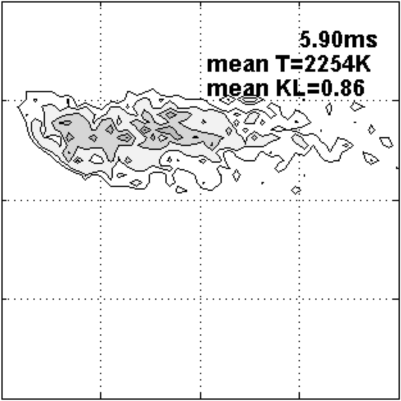

5.90ms
mean T=2254K
mean KL=0.86

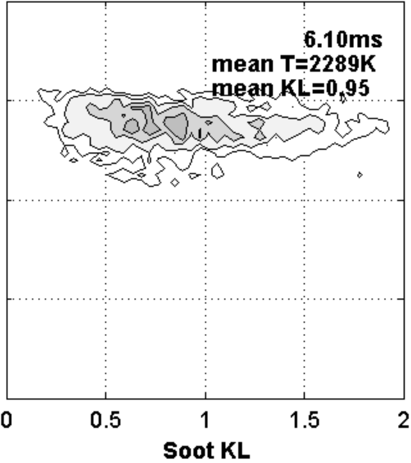
6.10ms
mean T=2289K
mean KL=0.95
0
0.5
1
1.5
2
Soot KL